Universitat Autònoma de Barcelona

Doctorat en Enginyeria Electrònica

Departament D'Enginyeria Electrònica

Array of microfluidic beam resonators for mass sensing applications - Design, Fabrication and Testing

Doctoral Thesis – July 2016

Salomón Elieser Marquez Villalobos
Author

Prof. Laura M. Lechuga Gómez
Director

Dr. Mar Álvarez Sánchez
Co-director

Dr. David Jiménez Jiménez
Tutor

CSIC
Consejo Superior de Investigaciones Científicas

ICN2
Institut Català de Nanociència i Nanotecnologia
Excelencia Severo Ochoa

Chapter 4 Chip packaging and optical readout

In the previous chapter we have presented three fabrication schemes employed to build embedded microchannels into doubly clamped beam resonators. Up to this point, the characterization of the HMB devices has been done mainly through visual inspection using an optical microscope and SEM micrographs to check specific characteristics such as dimensions, topology, surface planarization and porosity, undercut and integrity of the resonators. Nonetheless, it is important to compare and evaluate the results derived from the theory and simulation chapter with respect to the real response and behaviour of the fabricated resonators under operational conditions. Particularly, we must demonstrate the proof of concept of the sensor for measuring the viscosity and density of fluidic samples.

For this purpose, we have used the dynamic operational mode to evaluate the performance of the HMB sensor devices in order to study their mass responsivity, resonance frequency response and quality factor. Essentially, the gain spectral frequency of the driven response of the resonators oscillating in their fundamental mode should be rapidly detected to continuously follow the shifted frequency of the vibrating structures while streaming liquid solutions inside of the resonators. Consequently, the main prerequisite was to develop a suitable experimental setup for delivery of liquid samples, throughput excitation of the resonators and also for the acquisition and processing of data in real-time.

The description of the work done in this chapter is divided in two main sections: i) the development of the polymer-based bonding strategies and the integration of the fluid delivery system and ii) the full implementation of the experimental setup. In the first section, we explain two methodologies to integrate on-chip microfluidics with the second generation of HMB devices using two polymers: PDMS and SU-8. HMB devices of the first generation were exclusively employed to calibrate the measurement system due to their good resonance response. Whereas for the third generation of HMB devices, the fluid delivery channels were already integrated during the fabrication process, as described in the previous chapter. Next, the fluid delivery system for injecting fluids inside the resonators is outlined for HMB devices of the second and third generation. For this purpose, two holder supports were fabricated to integrate the microfluidic interconnections, the temperature controller and the elements for the active actuation of the resonators. In the second section, we describe in detail the components of the experimental setup and the optical readout to measure the driven resonance response of the resonators and their quality factors.. Finally, the last section

analyses the minimum detectable signal achievable by the interferometric setup along with a noise analysis of the experimental readout of the resonators.

4.1 Fluid delivery system integration: polymer-based bonding strategies

The microfluidic integration of the HMB devices of the second generation was challenging because of the intrinsic properties of the structural material, the morphology of the microstructures and the close proximity of the microfluidic inlets to the sensing area. As explained in the fabrication chapter, polycrystalline silicon possesses a rough surface consisting of grains of different size and directionality which can lead to poor adhesion with other substrates. Moreover, typical bonding methods that activate the surface of the substrates using plasma or corona treatments [1], [2] were not suitable here because the microstructures protruded out from the substrate (about 5 µm) which yielded bad sealing and leakage of liquids. To overcome these circumstances, we have implemented two polymer-based approaches for packaging our devices and thus facilitating the injection of fluids inside the HMB resonators. Both strategies effectively isolate the sensing area from the fluid delivery system and demonstrate a good step coverage of the microchannels topology. Furthermore, the polymers transparency is advantageous to integrate our devices with optical detection methods. Fig. 4–1 shows the two strategies for integrating polymer-based microfluidics with the second generation of HMB devices.

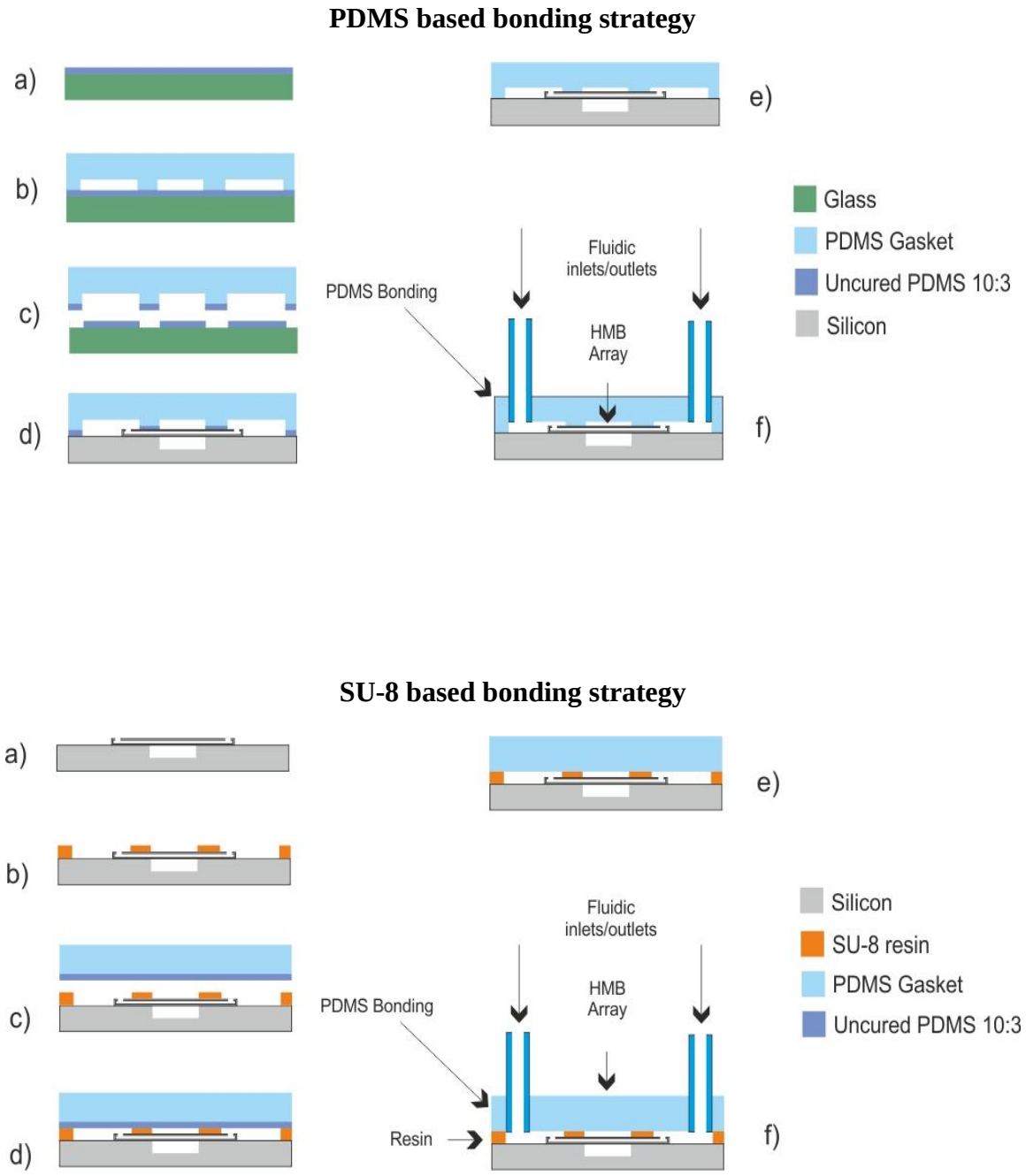

Fig. 4–1. Two approaches to integrate microfluidics with the second generation of HMB devices. (*Top*) a 10:3 PDMS is used as an intermediate adhesive layer to bond a PDMS gasket with integrated microfluidic channels to the devices. (*Bottom*) a SU-8 based microfluidic configuration is patterned onto the devices and sealing of the microchannels is done using a PDMS slab. Again, an uncured 10:3 PDMS layer is used as an intermediate adhesive.

4.1.1 PDMS packaging

The first methodology is based on a patterned PDMS gasket that incorporates the microfluidic bypass channels to deliver the liquid sample to the HMB resonators. The PDMS replica is obtained from a SU-8 master mould. Then, the polymer is aligned and permanently bonded to the surface of a single device based on a bonding strategy proposed by Gajasinghe et al. [3]. A thin layer of uncured PDMS with a curing agent ratio of 10:3 is used as an intermediate layer to bond the polymer microfluidics to the devices. In our approach, this bonding strategy consisted of four main steps: 1) fabrication of the master mould, 2) replica of the PDMS gasket, 3) alignment of substrates and, 4) permanent bonding.

The master moulds were fabricated using a SU-8 negative photoresist (Microchem SU-8 2025). Deposition of the polymer was based on the protocol provided by Microchem [4] to obtain a layer thickness of approximately 35 µm. Importantly, several conditions were optimized in the fabrication protocol according to our materials and facilities to build SU-8 master moulds with high endurance and thickness reproducibility. The design of the mask, which integrates the microfluidic configuration, was done in CorelDraw and printed on an acetate mask with MFS of 7 µm. Basically, two types of microfluidic designs were drawn for injection of fluids: in-line and H-shaped microchannels, as Fig. 4–2 shows. The in-line configuration has single input/output microchannels with reservoirs of 1.5 mm in diameter for direct injection of fluids into the inlets of the HMB resonators. On the other hand, the H-shaped configuration incorporates two bypass channels across each fluidic entrance of the resonators. The width of these channels is 200 µm. A central grid of 500 µm width is drawn in the middle of the mask to uncover the sensing area and avoid direct contact of the PDMS replica with the resonators. Both designs incorporate alignment marks to facilitate the alignment of the PDMS replica with a single device.

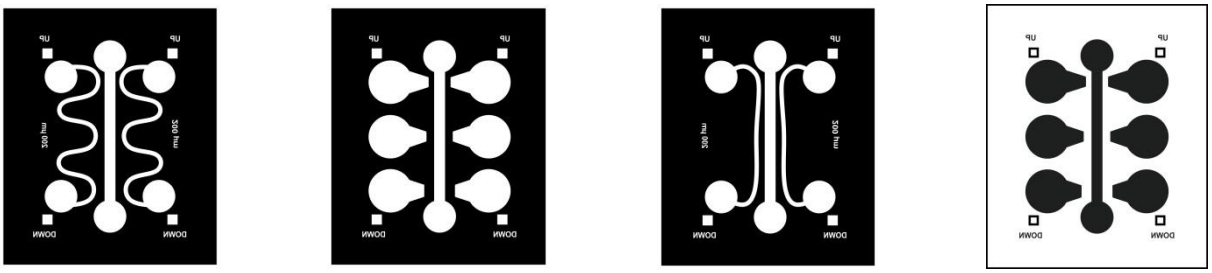

a) b) c) d)

Fig. 4–2. a) - c) Various mask designs for the SU-8 master mould that include in-line and H-shaped microfluidic configurations. Square alignment marks are located at the four corner sides to facilitate the PDMS replica bonding to a single device and d) positive mask design to transfer the polymer-based microfluidics directly on a single chip.

Table 4-1. Parameters of SU-8 spin coating process to obtain a thickness layer of ~35 µm.

Factor	Level 1	Level 2
Speed	600 rpm	3000rpm
Acceleration	600 rpm s^{-1}	600 rpm s^{-1}
Time	10 s	40s

For the fabrication of the SU-8 master moulds, 4-in type P silicon wafers of 300 µm thick with a resistivity of 5-10 ohm-cm were manually diced to have substrates with height and width of 30 mm and 25 mm, respectively. The silicon substrates were immersed in boiling piranha solution [H_2O_2: H_2SO_4 1:3] for 1 hr at 80°C to remove any organic residue, rinsed several times with distilled water and dried with air. Then, the Si substrates were dehydrated in an oven at 200°C for 30 minutes to improve the SU-8 film adhesion. 2.5 ml of SU-8 were dispensed onto the center of the substrates using a syringe; this strategy reduced the chances of bubble formation while depositing the resin. To obtain a uniform layer of about 35 µm, the SU-8 epoxy was spun using the parameters shown in

Table 4-1. Afterwards, a soft-baked of the samples was done in three different steps on a hot-plate to remove solvents and improve adhesion of the SU-8 layer: step 1 at 65 °C for 5 minutes, step 2 at 95 °C for 3 minutes and step 3 at 65 °C for 5 minutes, respectively. The microchannels were patterned by soft-contact photolithography with a Süss-Microtech MA 1006 aligner using the photomask design. According to the required thickness of the SU-8 film (~35 µm), an energy dosage in the range of 150-215 (mJ/cm^2) was used with an exposure time of 40 s to irradiate the samples.

Thereafter, a post exposure bake (PEB) improved the crosslinking degree and stabilized the irradiated zones. The PEB was carried out in three steps: the first step was done at 65°C for 3 minutes, the second step at 95°C for 5 minutes and the last step at 65°C for 3 minutes. The SU-8 film was developed by immersing the samples in metroxy-2-propanol acetate for 5 minutes at room temperature. Then the samples were rinsed with isopropanol and dried with air. To harden the resist an additional hard-bake step was performed at 150°C for 10 minutes on a levelled hot plate. Measurement of the microchannels thicknesses was taken from the samples at different locations across the width of the channels using the profilometer (KLA-Tencor P15), as Fig. 4–3a,b shows. In sum, the average SU-8 film thickness was ~34.08 µm with a standard deviation of 1.59.

The 4 mm thick PDMS replicas were prepared by a 10:1 ratio of elastomer and curing agent from “Sylgard 184 Silicon elastomer Kit”. The mixture was poured into a methacrylate mould that contained the SU-8 master mould, as Fig. 4–3c shows. The PDMS was then cured in a levelled hot plate at 80°C for 2 hrs. Thereafter, the PDMS replica was unmoulded from the methacrylate mould and four through holes were perforated on each reservoir with a biopsy punch (Harris Uni-CoreTM 1 mm I.D.) for external access of tubing connections. Finally, the PDMS was cut to have dimensions of 1 x 1 cm using a razor blade.

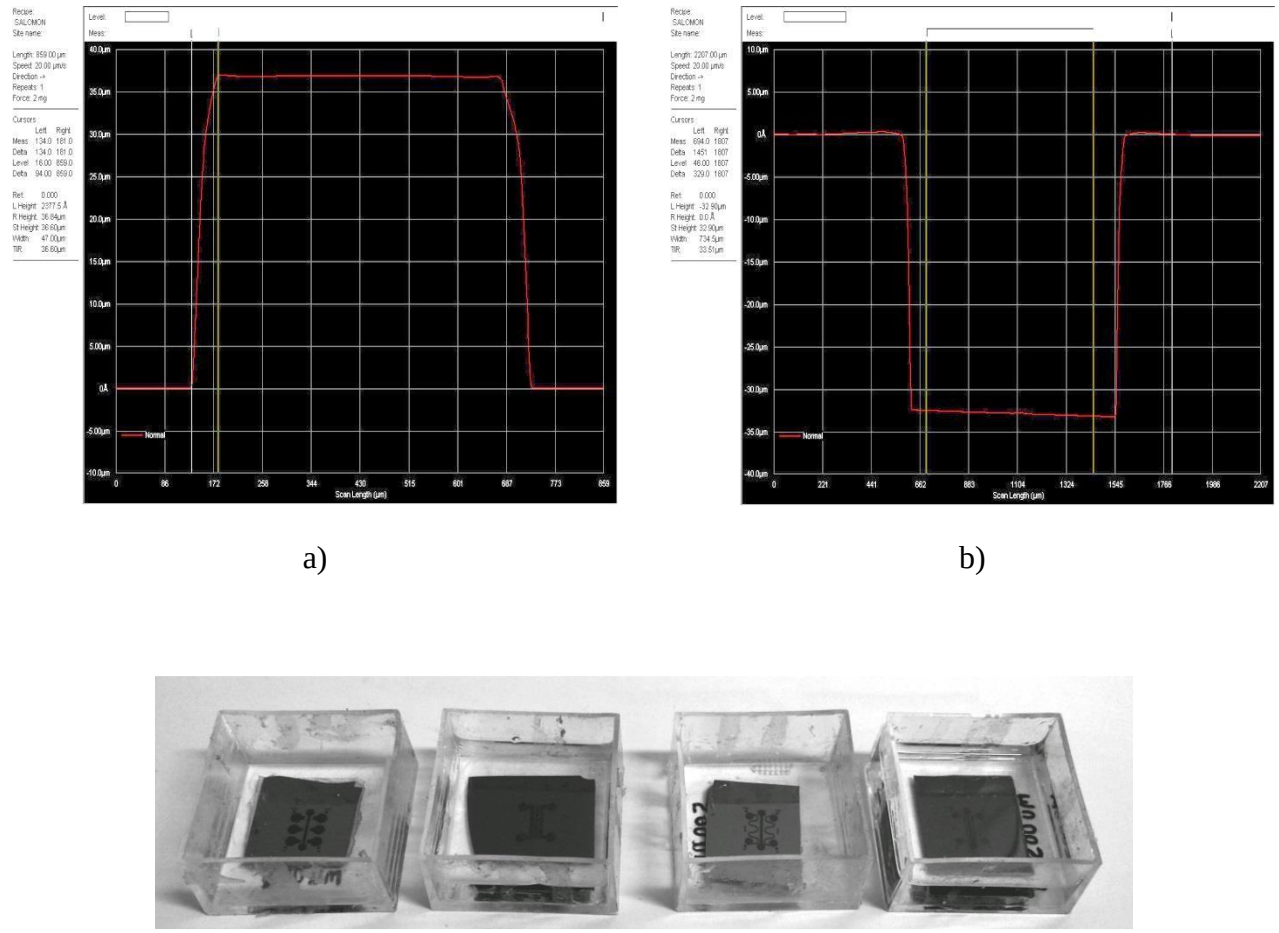

a) b)

c)

Fig. 4–3. Microfluidic channel profile measured with a profilometer. a) Positive master mould of SU-8 showing a step height of about 36 µm, and b) negative master mould patterned on an HMB device to integrate the microfluidic channels directly on the chip. Edge beds at the corners of the channels are common when thin-films of SU-8 are deposited. c) Methacrylate moulds that contained different SU-8 master moulds in which the bypass microfluidic pattern is transferred to a 10:1 PDMS replica.

Next, uncured PDMS with a mixing ratio of 10:3 was spun over a thin glass slide at 4000 rpm for 30 s. These spinning conditions were applied to obtain a thin PDMS layer of about 4 µm [3]. Then, the PDMS replica was placed over the uncured 10:3 PDMS layer with the microfluidics pattern facing towards the slide. Gentle pressure was applied atop the mould to allow the full coverage of the uncured polymer over the replica surface and also to get rid of trapped air bubbles. Then, the PDMS replica was carefully removed from the slide using fine tweezers and deposited upwards into a new cover slide to avoid clogging of the microchannels.

The alignment of both substrates proceeded as follows. Fig. 4–4 shows a setup that allowed us to correctly align the polymer microfluidics to the HMB devices. Basically, the setup incorporates eight degrees of freedom to monitor the alignment process of both substrates with a microscope camera; it also includes a temperature controller and a vacuum inlet to avoid the movement of the chip. First, the PDMS replica along with the cover slide was placed on the upper part of the setup in such a way that the microfluidic pattern was facing downwards. The PDMS gasket was partially bonded to the cover slide by means of Van der Waals forces. The chip was then placed underneath the PDMS replica and fixed using vacuum; both substrates were positioned facing to each other and the four alignment marks were used to visually monitor the alignment process. When the alignment was completed, the substrates were put into contact allowing that the uncured PDMS slightly covered the whole device surface as Fig. 4–5a shows. The vacuum was then stopped and the HMB device was allowed to be attached to the PDMS replica. We noticed that adding soft pressure to make the bonding process faster resulted in reflow of the uncured polymer, as Fig. 4–5b shows. Any temperature increase during the curing process led to clogging of the microchannels(see Fig. 4–5c) . Once the uncured PDMS spread all over the surface, the glass slide along with the bonded substrates was removed from the setup support and the 10:3 PDMS was cured for 48 h at room temperature. Finally, four PEEK (Polyether Ether Ketone) tubes (Valco Instruments Co. Inc. JR-T-6009) of 250 µm of i.d. were affixed to each reservoir to complete the integration of microfluidics. Fig. 4–5d-f illustrates the chip device with integrated microfluidics.

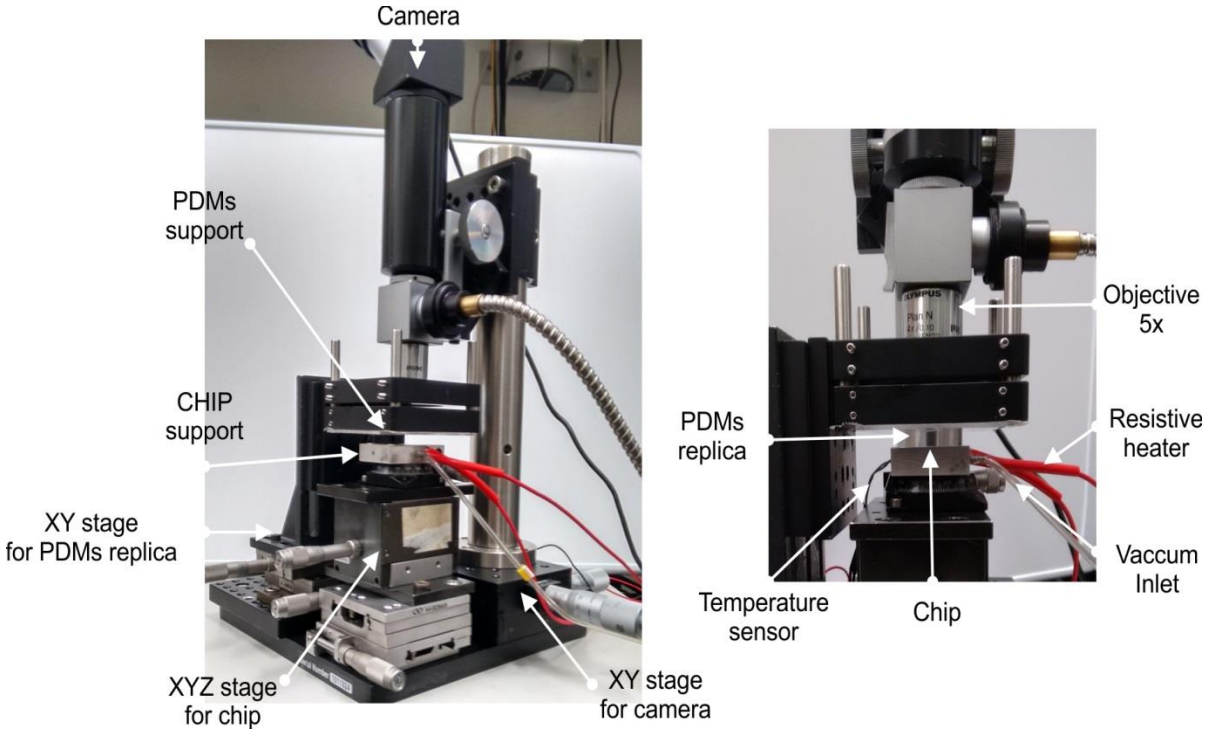

Fig. 4–4. Setup to align the PDMS replica with the patterned microfluidics to the HMB devices. The setup incorporates eight degrees of freedom to properly incorporate the microfluidic pattern to the chip under a microscope camera. Temperature stabilization and vacuum are included to monitor the bonding process.

This bonding strategy used PDMS with a curing agent ratio of 10:3 as a glue to stick PDMS moulds to the HMB devices. For the case of polycrystalline silicon substrates, the resulted bonding was permanent. The maximum pressure that this permanent union can stand is up to 38 psi, which is adequate for flow rates below 100 µL/min [3]. The bonding showed good step coverage over the microchannels by effectively isolating the sensing area from the fluid delivery network. Moreover, the bonding strategy was carried out without applying additional pressure and at room temperature reducing the changes of the uncured PDMS to reflow. Hence, this methodology resulted effectively to integrate microfluidics on our HMB devices.

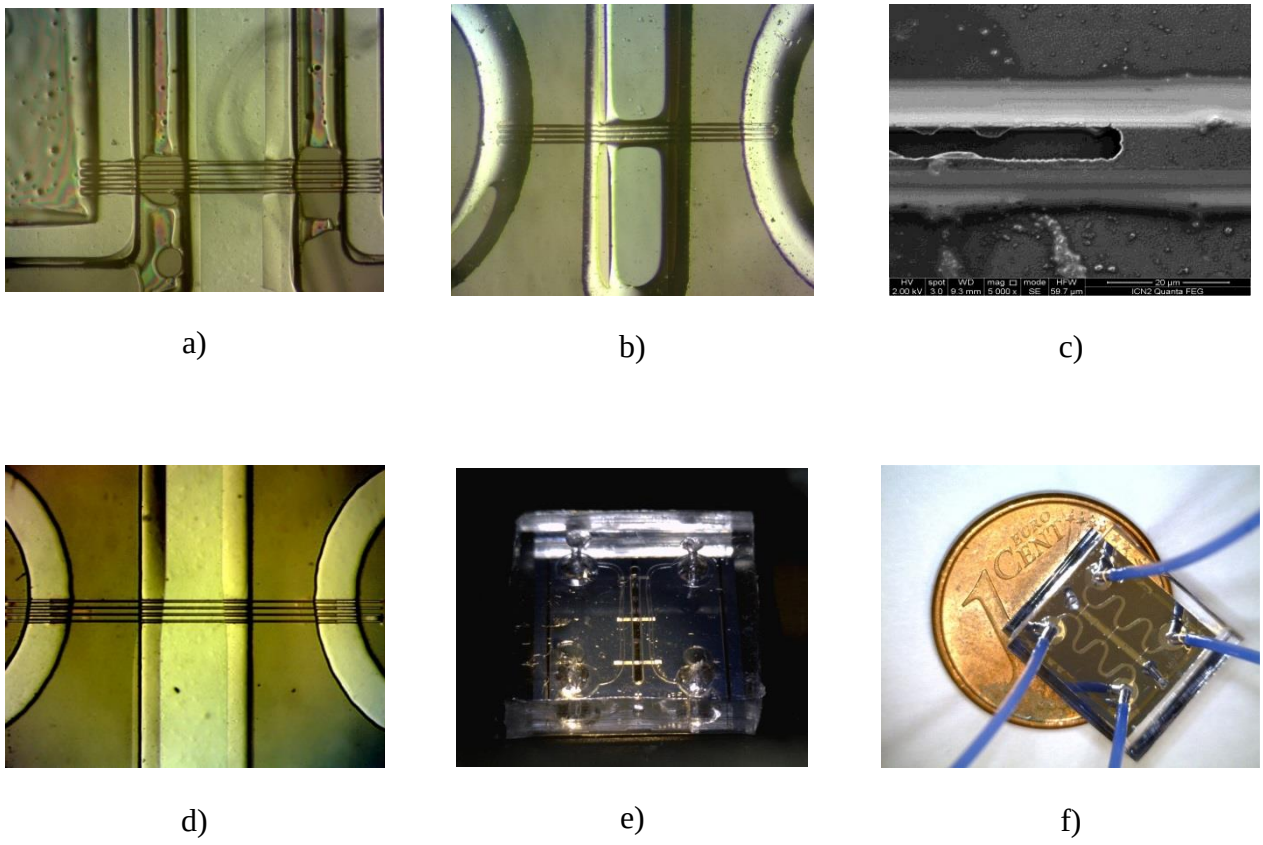

Fig. 4–5. a) Uncured PDMS is allowed to spread and cover the microchannels to correctly define the sensing area of the sensor from the fluid delivery channels, b) excess of pressure resulted in clogging of the bypass microfluidic channels, c) any increase in temperature caused the uncured PDMS to reflow, d) - e) coating of thin layers of uncured PDMS yielding good sealing and step coverage of the microstructures and f) a device with integrated polymer microfluidics after the bonding process. Four PEEK tubes are plugged into each reservoir for exchange of the liquids.

4.1.2 SU-8 based packaging

The second bonding strategy consisted of spinning the SU-8 epoxy directly onto the HMB devices. The microfluidic pattern was transferred to the devices by soft-contact lithography using the acetate mask and the fabrication protocol described in the previous section. The patterned polymer microchannels were enclosed using a thin slab of 10:1 PDMS. To bond both substrates, uncured 10:3 PDMS was used as an intermediate bonding layer. Prior to the bonding process, the reservoirs were perforated for the injection of fluids. This methodology avoided the further alignment of the top PDMS lid to enclose the microchannels and therefore, a direct bonding of both substrates could be done manually. Finally, the 10:3 PDMS was cure over 48 h to complete the bonding process. Although this methodology reduced the usage of intermediate alignment methods, the topology of the structures was severely deteriorated.

As the beams were already released from the substrate, they were under compressive forces after depositing the SU-8 resin. During subsequent thermal processes, the solvents from the SU-8 resin evaporated and thus the exceeding stress damaged the resonators. Generally, bonding strategies based on adhesive tapes [5], UV photoresists [6] and usage of sticky PDMS as adhesive [7] are not convenient because the intermediate bonding layer has to cover the complete sensing area affecting the integrity of the sensor. Moreover, the resin can reflow and destroy the patterned microchannels. Resin residues can also fill the microchannels by capillary forces and yield clogging. In our case, the SU-8 material was easily removed from unexposed zones before the bonding step by over-exposing the samples with the developer agent. Another important aspect of the patterned SU-8 channels was with respect to its surface planarization. The surface of the SU-8 resin was not uniformly distributed throughout the chip; in particular, edge beads were formed along the edges of the devices. This non-uniformity reduced the contact surface of the PDMS lid producing a low bonding strength. Fig. 4–6 shows the surface of the SU-8 resin deposited on a single device; the microscope image shows good step coverage of the resin, but the integrity of the microchannels is clearly affected. Hence, this method did not prove to be useful for integrating the microfluidics in our devices.

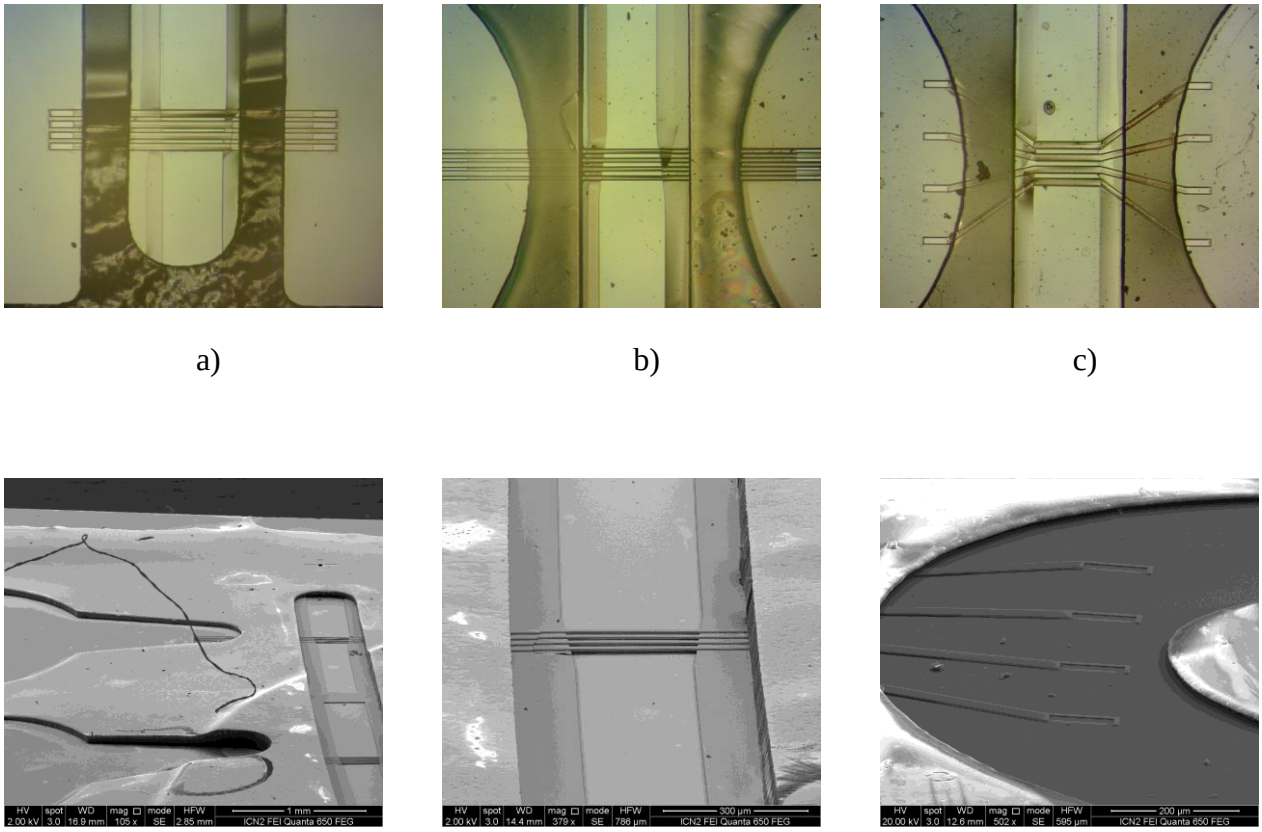

a) b) c)

d) e) f)

Fig. 4–6. a) - c) Microscope images of devices with patterned SU-8 microfluidic channels. Isolation of the sensing area was effective but the integrity of the suspended structures was affected. Differences in the colour of the resin indicate a non-uniform deposition of the SU-8 layer and d) - f) SEM micrographs of edge beads along the microchannels. The deposited resin rendered in good step coverage over the microchannels but it was necessary to optimize the development process to avoid any traces of resin over the unexposed areas.

4.2 Experimental setup implementation

4.2.1 Chip packaging: electrical and microfluidic interconnections

4.2.1.1 Assembly of the second generation of HMB devices

After integrating the polymer-based microfluidics with the HMB devices of the second generation, it was necessary to adapt the external fluidic interconnections for the exchange of fluids inside the embedded microchannels. In the following, we explain in detailed the elements employed to integrate the external fluidic interconnections, to establish the temperature control of the system and to place the piezoceramic crystal for actuating the resonators. All the elements were incorporated into a holder support which was mounted on an XYZ stage. The stage was used to align the laser spot onto the midspan of the resonators. Fig. 4–7 illustrates the holder support for these type of devices.

The temperature control of the system included a peltier module (Thorlabs TEC3-6), a temperature transducer (Thorlabs AD590) and a closed loop temperature controller (Thorlabs T-Cube TEC Controller) with a resolution of 0.1^{o} C. A copper fixture housed the peltier module, the temperature transducer, and also the piezoceramic crystal; copper material was used because of its high thermal conductivity (385 W/m K). As shown in Fig. 4–7, the HMB device with integrated microfluidics and external tubes was placed directly on the piezoceramic crystal for mechanical actuation of the resonators. The chip was attached to the holder support using a 3D printed plastic lid and four bolts. As the thickness of the PDMS gasket was about 4 mm, the HMB device could be tightly fixed to the holder support without causing any damage to the microchannels. In this way, the laser spot could be focused directly onto the resonators through the PDMS gasket since this material is transparent at wavelengths of 633 nm.

The filling of the embedded microchannels was done using two approaches: H-shaped and in-line microfluidic configurations, respectively. For the first approach, 250 µL of sample volume were loaded and delivered into one of the bypass channels by a low-pressure valve (Valco Instruments Co. Inc. C22-3186) at a constant flow rate of 10 µL/min using a syringe pump (New Era Pump Systems Inc. NE-300). On the other bypass channel, a constant flow rate of 1 µL/min rinsed the output of the microchannels continuously by using another syringe pump. For the in-line approach, the sample fluid was delivered into one of the inlet reservoirs at constant flow rate of 5 to 10 µL/min using a single syringe pump. Before measuring a sample, the microfluidic channels were cleaned with sodium dodecyl sulphate (SDS), hydrochloric acid 0.1 M (HCl) and rinsed with plenty of water to reduce systematic instabilities on frequency. Finally, the temperature of the sensor was stabilized at 23^{o} C by the temperature controller. Measurements were taken after 5 min of sample injection to ensure complete liquid exchange inside of the resonators and temperature stabilization. All measurements were done at least in triplicates.

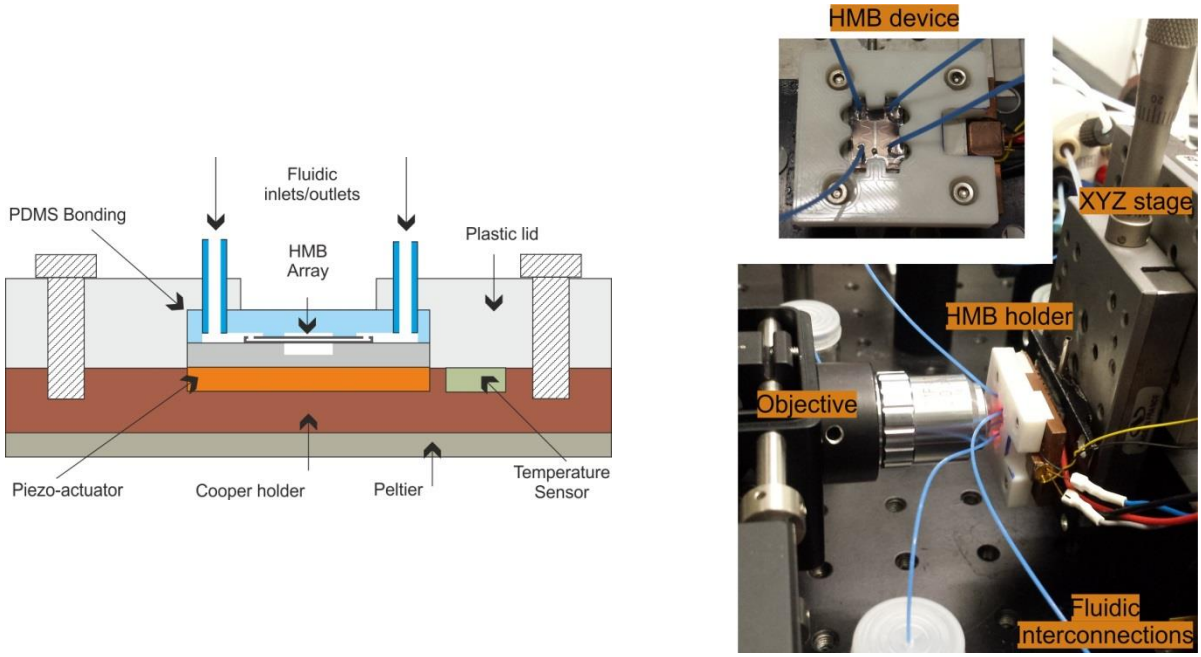

Fig. 4–7. A fixture of copper houses a peltier module, a temperature transducer and a piezoceramic actuator for driving excitation of resonators at a fixed temperature, while streaming various sample solutions. The stage was used to align the laser spot onto the midspan of the resonators.

4.2.1.2 Assembly for HMB devices of the third generation

For the assembly of the third generation of HMB devices it was necessary to build a new holder support given that the fabrication of the devices included bulk micromachining and the polymer-based microfluidics was already integrated on the front side. Several considerations were taken into account for the design of the new holder: 1) the injection of fluids inside the HMB devices had to be done through access through-holes located underneath the chip, 2) the material of the holder support should be transparent to allow direct focusing of the laser beam, 3) it should incorporate the elements for actuation of the resonators and finally 4) it had to include a vacuum inlet to study the response of the resonators at different pressures. Fig. 4–8 shows the holder support designed and built in our mechanical workshop using a CNC (Computer Numerical Control) machine. The new holder was made of methacrylate material and consisted of two main parts. The lower support incorporated the external tubing connections for fluid exchange inside the resonators. It also housed the piezoceramic crystal for actuation of devices. The upper support enclosed the lower support creating a small chamber for performing a partial vacuum on the microstructures.

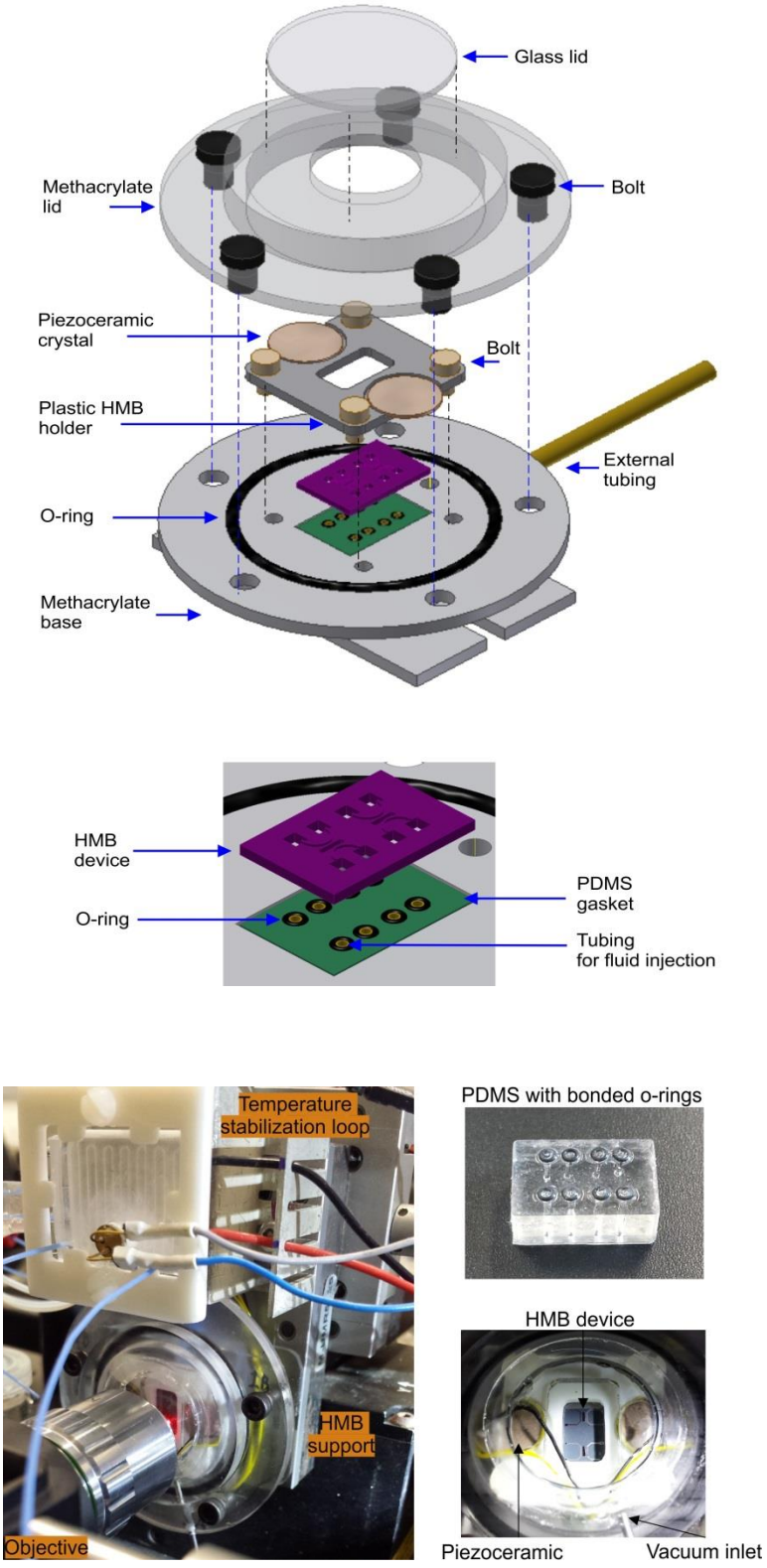

Fig. 4–8. Methacrylate holder support for HMB devices with integrated SU-8 polymer microfluidics. The injection of fluids is done underneath the chip through a PDMS gasket which includes O-rings at each reservoir for leak-free connections. The piezoceramic actuators are placed on top of the devices. The support also integrates a vacuum inlet.

Incorporating the injection fluid ports along with partial vacuum of the HMB devices was a challenge. The eight microfluidic inlets of the HMB devices had to be perfectly sealed to reduce the leakage of fluids while performing vacuum inside the holder support. To overcome this situation, we used O-rings for each microfluidic reservoir. The O-rings were bonded to a 4 mm thick PDMS gasket with a curing agent ratio of 10:1, as Fig. 4–8 shows. The PDMS replica was obtained from a methacrylate master mould that included the dimensions and location of each microfluidic inlet to facilitate the alignment and placement of the HMB devices. Also, the PDMS mould was used for connecting eight PEEK tubes at every microfluidic inlet for the exchange of fluid samples. Afterwards, the tubes were folded 90^{o} towards the exterior fluidic interconnections. All possible air leaks were sealed with UV epoxy. Mechanical actuation of the resonators was done using piezoceramic crystals located on top of the HMB device. In this design, the actuation scheme could not be integrated under the microstructures because of the fluidic interconnections located beneath the device. The piezoceramic crystals were housed and glued to a 3D printed plastic lid, as Fig. 4–8 shows. Afterwards, the HMB device was placed onto the PDMS gasket with the integrated O-rings. The HMB chip was attached to the lower support holder using the plastic lid and adjusting four bolts to improve the contact and sealing of the microfluidic inlets. A small through-hole was perforated on the lower support for the electrical connections of the actuators. This hole was further sealed with UV epoxy to avoid air leaks.

Access to the vacuum inlet was included on the upper support of the holder. The small chamber that contained the HMB devices had to include an air extraction inlet to study the influence of the pressure on the quality factor and frequency of the resonators. Therefore, an O-ring of 2.2 cm of diameter along with five bolts was used to ensure a good sealing of the two supports. On the other hand, given that methacrylate material can cause the laser beam to diffuse, an access through-hole was perforated on top the upper support. A thin glass cover was bonded to the upper support using a UV polymer to properly enclose the chamber. In this way, the laser beam was focused onto the microstructures through a thin glass cover to reduce light losses. We also incorporated a temperature control for the fluid sample instead of stabilizing the temperature of the HMB devices. Thus, the temperature control implemented for HMB devices of the second generation was reutilized, but with slight modifications. A microfluidic design was patterned on a PDMS mould using the fabrication procedures already described. The design consisted of a serpentine shaped microfluidic channel of 200 μm height and width with a total length of about 5 cm. After perforating the reservoirs, the PDMS mould was permanently bonded to a thin slide of glass using oxygen plasma. The dimensions of the PDMS mould included the whole surface of the peltier module to enhance the contact surface during the temperature stabilization of the fluid sample. The temperature transducer was fixed on the front the PDMS gasket using a conductive paste, as Fig. 4–8 shows. A 3D printed plastic lid was used to attach the PDMS mould along with the cover slide to the peltier module; meanwhile, an aluminium dissipator was placed on the other side of the peltier module. Finally, PEEK tubes were affixed to each reservoir for direct injection of liquid phase fluids. The temperature of the samples was stabilized at 25^{o}C prior the filling of the HMB devices.

4.2.2 Interferometric readout

In our approach, we measured the bending motion of the beam structures by implementing an interferometric readout based on a Michelson interferometric setup configuration. Fig. 4–9 shows a detailed description of our homebuilt experimental setup. A 632.8 nm HeNe laser beam of 1 mm diameter (JDSU 1101, 1.5 mW) passes through an optical isolator (Thorlabs IO-3D-633-VLP) to cancel undesired back reflections and noise fluctuations. The optical isolator is aligned so that the incident light is polarized along the axis of the beams, which has shown an enhancement in the scattered intensity for nanostructures [8]. A 50:50 beamsplitter (Thorlabs CM1-BS1) splits the laser beam in two beams to form a reference path, which reflects back from a reference mirror onto a high bandwidth photoreceiver (New Focus 1801). The distance of the reference mirror is set as close as possible to the beamsplitter (5 mm). On the active arm of the interferometer, the beam is expanded five times with a beam expander (Thorlabs BE05M-A) for imaging purposes and for reducing the final spot size. To prevent heating of the resonators, a neutral-density (ND) filter is used at the output of the beam expander to control the intensity of the laser beam. Thereafter, the laser beam is focused tightly through a microscope objective (Olympus 20x, NA = 0.4) onto the middle of the resonators. The spot size of 1.3 µm is calculated according to the Rayleigh criteria: $\omega_0 = 1.64\lambda/2NA$ where diffraction is avoided given the tightly focused spot onto the structures.

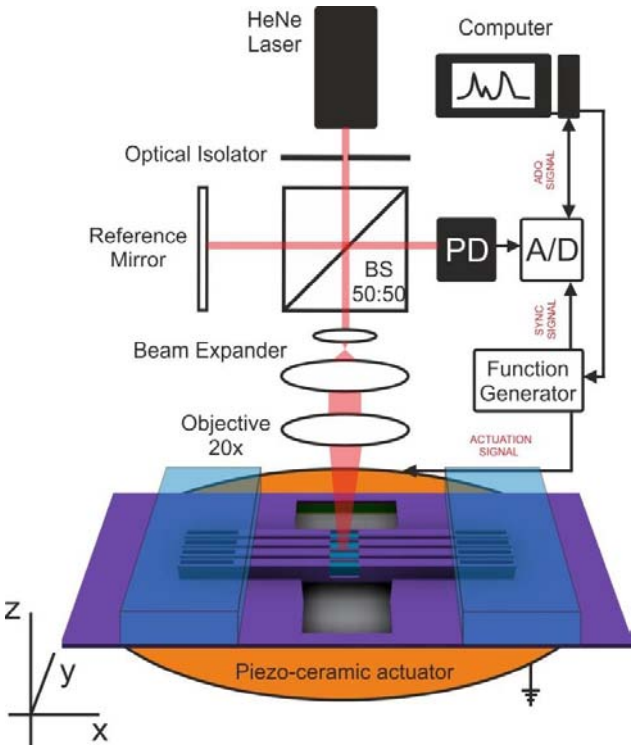

Fig. 4–9. a) Schematic view of the functionality principle of the HMB resonator and the experimental setup. A custom free-space interferometer acquires the driven excitation response of resonators while a sample solution is streaming through the embedded microchannels.

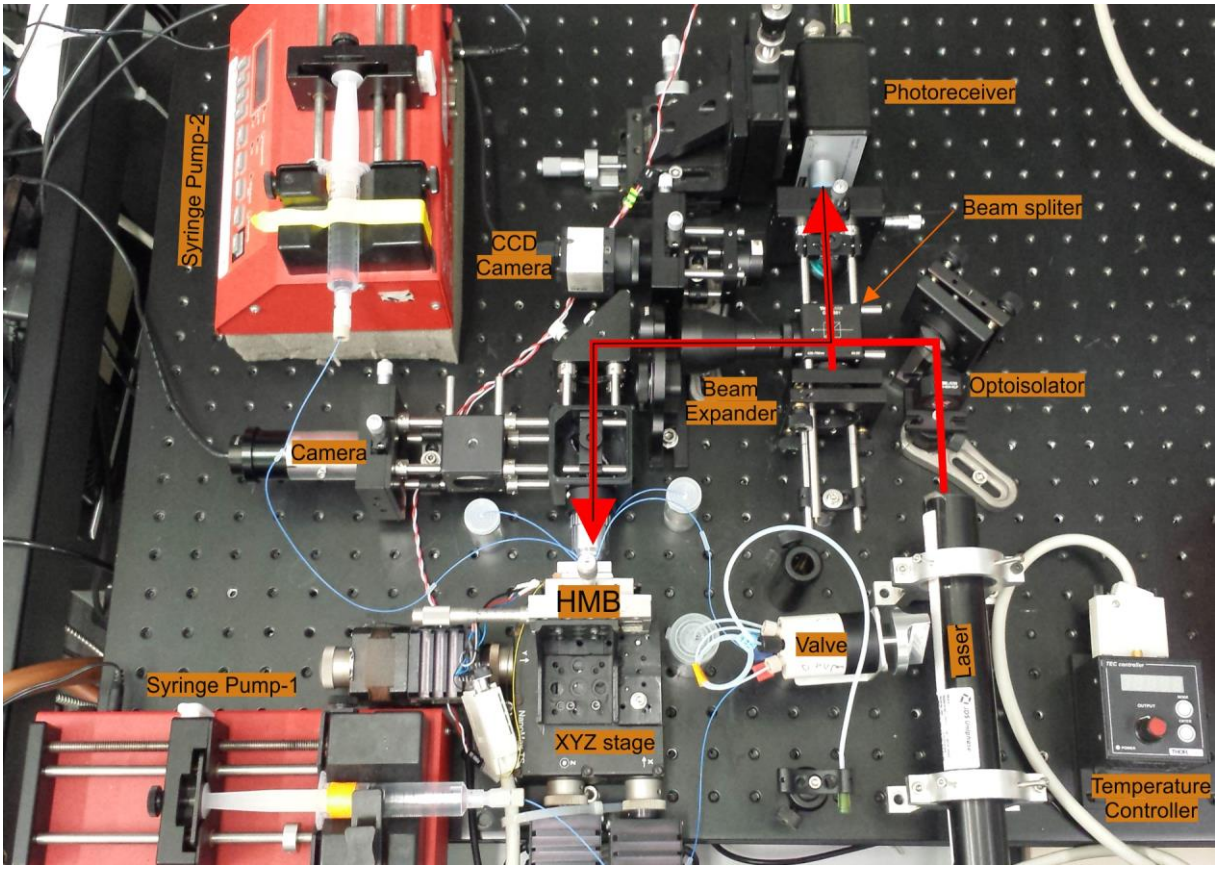

Fig. 4–10. Experimental setup that includes the Michelson interferometer, actuation and excitation of the resonators, and fluid delivery interconnections. All optical components are rigidly assembled to an optical table with active mechanical isolation.

The photoreceiver further collects the interference pattern due to the reflected light from a single beam and the light from the reference mirror. In addition, the setup incorporates two reference arms to facilitate the alignment of the interference pattern and also to focus the laser beam onto the midspan of the resonators. The first arm directs 8% of the beam intensity, reflected back from the microstructures, to a microscope camera using a beamsplitter (Thorlabs BP108); in this way, the middle point of the doubly clamped beams can simply be aligned with the laser beam spot. The other arm is located just before the input of the photoreceiver and it consists of a CCD camera that collects images of the interference pattern for alignment purposes by using a dichroic mirror aligned at 45^{o} (Thorlabs DMLP638). All optical components are rigidly assembled to an optical table with active mechanical isolation to compensate for undesired vibration drifts(see Fig. 4–10).

4.2.3 Actuation and acquisition schemes

The actuation of the array of resonators was done through a frequency sweep methodology that allowed a fast and high-throughput excitation over a range of frequencies around the central peak response of the resonators. This methodology has been successfully applied for fast frequency sweeping in resonance-tracking of scanning probe microscopy (SPM) for high-resolution imaging [9]. In our approach, the excitation was performed by a piezoceramic actuator (PImicos PIC181) placed beneath the chip to acoustically actuate the resonators using a function generator (Agilent 33220A), as Fig. 4–9 shows. The function generator controlled the amplitude, frequency bandwidth and sweep time of a sine-wave excitation signal around the central peak response of the resonators. The driven response of the resonators was acquired by a synchronization protocol between the function generator and an acquisition card (National Instruments PXI-5922) to avoid cross-talk of the collected signals by the photoreceiver. Real-time processing of the signals was done in a graphical programming language (Labview) to obtain the gain frequency spectrum of the resonators. The computed Fast Fourier Transform (FFT) was averaged two times to reduce noise fluctuations and a Lorentzian curve fitting algorithm computed the peak frequency response and Q-factor values. Automatic sequential detection of every resonator response was performed by transversally scanning the complete array under the optical spot by a computer controlled 3-axis stage.

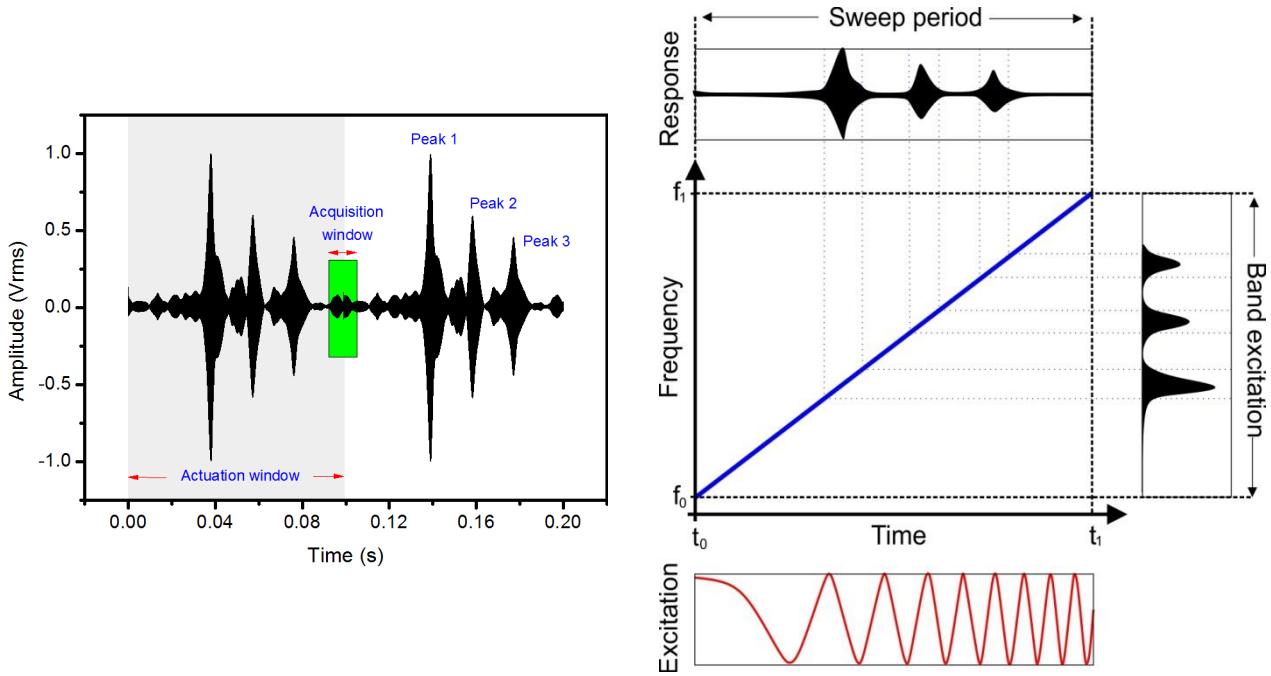

Fig. 4–11. Acquisition and actuation scheme to capture the frequency response of a HMB device o the first generation through a frequency sweep methodology that allowed a fast and high-throughput excitation over a range of frequencies around the central peak response of the resonators. Cross-talk of signals is impeded by using a synchronization protocol that captures samples (a 5 ms acquisition window) after each excitation sweep frame (sweeping period of 100 ms). Excitation of resonators is produced acoustically using a piezoceramic crystal. The amplitude, sweep time and bandwidth of the sine-wave excitation signal are controlled by a function generator.

The synchronization protocol consisted of acquiring the driven response of the resonators by setting a short acquisition window just between the beginning and ending of each excitation sweep period, as Fig. 4–11 shows. The main synchronization signal was provided by the function generator with a duration of 100 ms which was the time assigned for the band excitation sweep. For sweep duration of 100 ms, the stability of the peak amplitude was maintained as the rate of the sweeping time was faster, however, sweeping times below 100 ms induced lower amplitudes of the frequency spectrum. This can be explained because the time required for continuously driving the frequency response of a given resonator into resonance was lower.

Moreover, in order to optimize the timing response of the acquisition system, the duration of the acquisition windows was chosen in accordance to the relationship $T_{acq} = N_{samples}/F_{sample}$. Owing that the expected fundamental frequency of the resonators was between 400 KHz to 1 MHz, the sample rate (F_{sample}) of the fast acquisition card was set to 2.5 MS/s to capture frequency spectrums of up to 1.25 MHz (F_{sample}/2). For the selected sampling rate, three acquisition windows with duration of 5 ms, 10 ms and 20 ms were evaluated to determine the optimum number of samples per frame. As a result, the amplitude of the frequency spectrum increased as the duration of the acquisition window was reduced (less acquired samples per frame), as Fig. 4–12 shows. On the contrary, the width of the frequency peaks became wider for windows with a shorter duration. Thus, the duration of the acquisition window was set to 5 ms (equivalent to $N_{samples}$ =12,500) because frequency peaks with more stable and larger amplitudes were displayed. Finally, by locating the acquisition windows just right before each excitation cycle, the cross talk of the captured signals notably faded away.

To study the interplay between the frequency sweep bandwidth and the driven frequency peak of the resonators, various bandwidths were evaluated. Fig. 4–13a shows the response of a device with three bandwidths of 450 KHz, 500 KHz and 600 KHz, respectively. Notably, the length of the frequency bandwidth did not influence on the magnitude of the peak and stability response of the resonators. Differences in the amplitude of the spectrum were derived from artifacts or mechanical drifts of the interferometric setup. Furthermore, leaving a frequency gap of about 200 KHz around the central frequency peak of a single resonator was sufficient to cancel the cross-talk between the acquired and actuated signals.

For the online computing of the resonant frequency and energy dissipation of the resonators, the amplitude of the resonant peak response need to be stable to enhance the accuracy of the measurements. Therefore, the relationship between the amplitude of the actuation signal with respect to the amplitude of the spectrum was also studied. Fig. 4–13b shows the resonant peak magnitude of a resonator for actuation voltages of 0 Vpp, 5 Vpp and 10 Vpp, respectively. It can be observed that the amplitude of the spectrum linearly increased with respect to higher applied voltages. By performing this actuation methodology, the response of the resonators was assured within the linear regime. Finally, since the quality factors of the resonators computed by the nonlinear fitting algorithm depended on the amplitude of the frequency spectrum, the amplitude of the actuation signal was set to 5 Vpp for all the measurements.

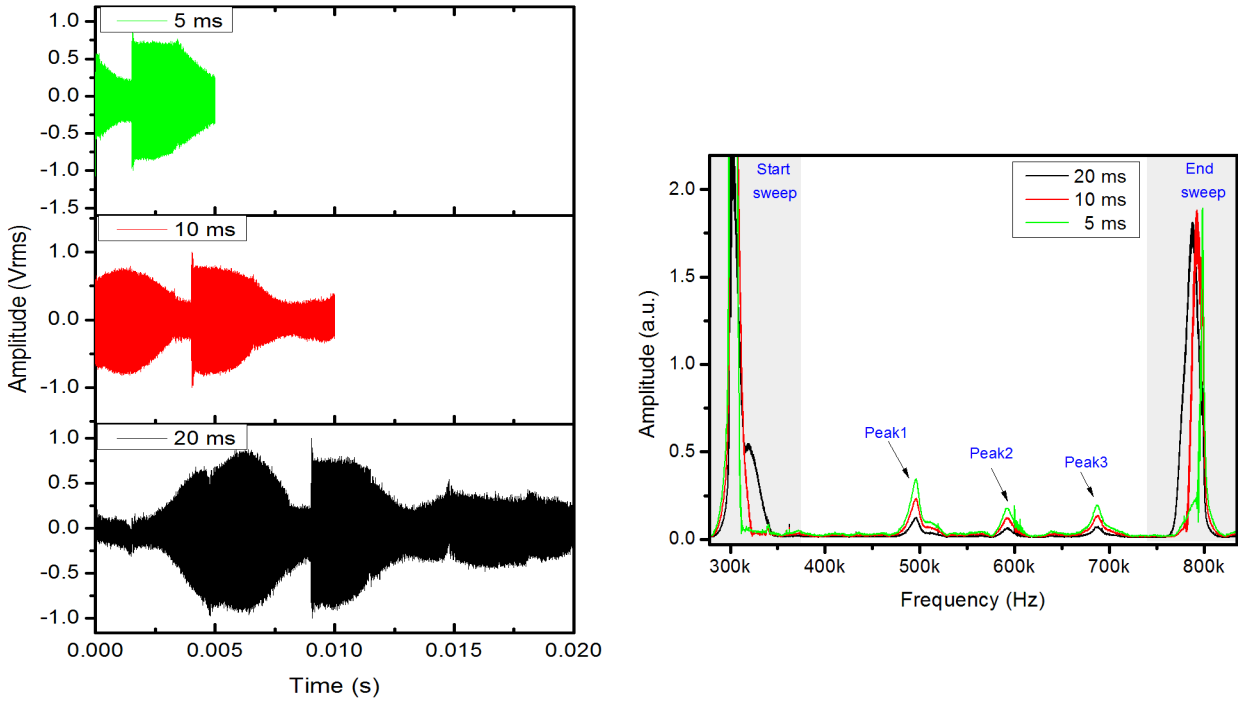

a) b)

Fig. 4–12. a) Plots of amplitude *versus* time to evaluate the effect of the acquisition window length over the frequency response of HMB resonators of the first generation. b) The amplitude of the frequency spectrum increased as the duration of the acquisition window was reduced (less acquired samples per frame). An acquisition window of 5 ms produced a more stable and constant amplitude response of the resonators

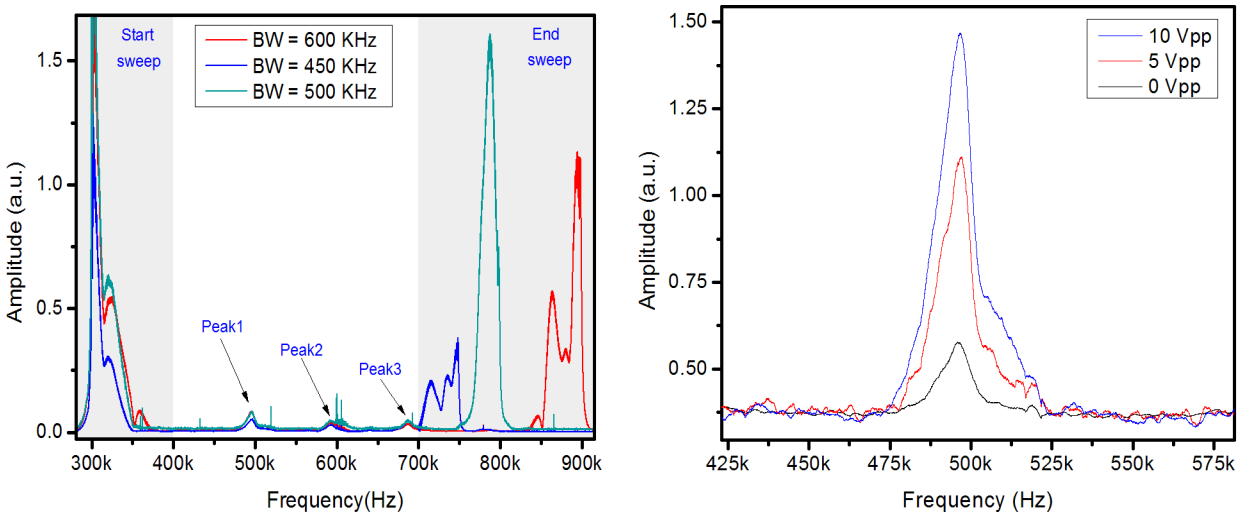

Fig. 4–13. a) Plots of the amplitude of the frequency spectrum versus different sweeping frequency bandwidths. The amplitude of the spectrum was not affected by the length of the frequency bandwidth. b) Amplitude of the frequency spectrum as a function of the applied voltage of the excitation signal.

4.2.4 Signal processing and graphical user interface

Fast and online tracking of the frequency response of resonators is crucial to resolve for mass and viscosity changes of the sensors while streaming various sample solutions. Therefore, we developed a graphical user interface (GUI) in Labview to characterize the response of the devices as can be seen Fig. 4–14a. The architecture of the program was based on an event handling methodology that allowed high performance and effective data synchronization. In real-time applications, it is important to avoid data losses while simultaneously acquiring and processing information. In our approach, four principal events were taken into consideration: data acquisition, processing of data (non-linear curve fitting), actuation control and data storage, as illustrated in Fig. 4–14b.

The program starts by defining and initializing the variables used in the program and the parameters corresponding to the configuration of the acquisition card and function generator equipment. The communication with the acquisition card was done through a serial interface for high-speed communication (via RS232 port) to define the number of channels, sample rate (2.5 MS/s), the number of samples frame (12500), voltage vertical range (5 Vpp) and external triggering signal. Meanwhile, the function generator was configured through the USB port through a Virtual Instrument Software Architecture (VISA session) to configure the linear sweep spacing, frequency bandwidth (about 400 KHz), sweeping time (100 ms) and excitation amplitude (5 Vpp).

Effective data synchronization is achieved through a producer/consumer configuration between the data acquisition and processing loops using a queue protocol. A queue is useful to avoid overflow and data losses while the acquisition loop is creating new data to be processed by the processing loop. The advantage of using a queue is that the producer and consumer rates do not have to be identical. Hence, every time that the queue overflows, a time delayed is programmed to make a complete processing of data before capturing new samples.

Once the elements are dequeued into the processing loop, the DC and AC response of the photoreceiver is obtained. The AC response is normalized and then the FFT is computed using a Hanning window. The resulted frequency spectrum is smoothed by applying an exponential RMS averaging two times. Afterwards, the software tracks the peak frequency shifts automatically but the user must provide a first approach of the central peak response of the resonator within a frequency bandwidth. A Levenberg-Marquardt algorithm computes the non-linear fitting of the frequency spectrum by employing the following formula:

$$X(f) = y_0 + \frac{A_0 f_0^2}{\sqrt{(f^2 - f_0^2) + \frac{f^2 f_0^2}{Q^2}}} \qquad \text{Eq. 4.1}$$

where f and f_0 are the drive frequency and resonance frequency, Q is the Q-factor, A_0 is the magnitude of the excitation and y_0 is the baseline offset. As Fig. 4–14 shows, the software displays

the temporal evolution of frequency and quality factor of the fitted spectrum. The excitation signal that induces the displacement of the resonators is activated by the user before initializing the acquisition of samples. Finally, the fitted values of the central frequency peak, amplitude, Q-factor and offset are saved into a file for further processing and interpretation. Although this approach resulted in high-throughput and fast excitation method for fast tracking response of the resonators, the accuracy of the method can be improved to resolve for smaller frequency shifts.

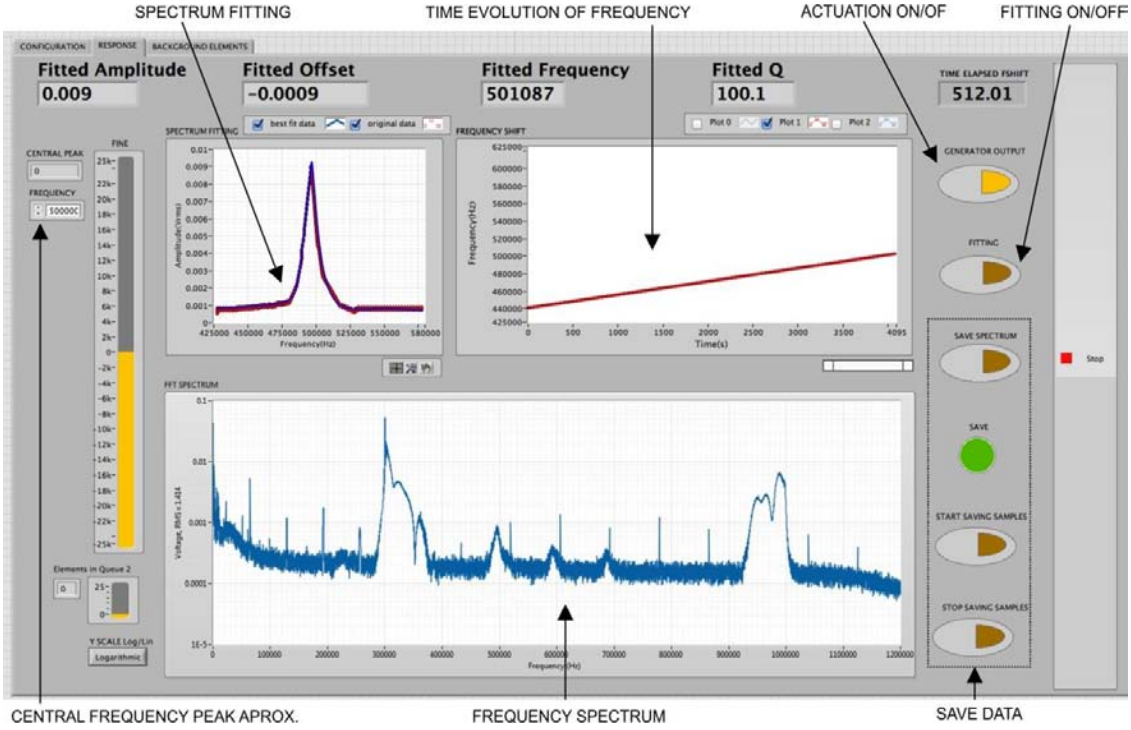

a)

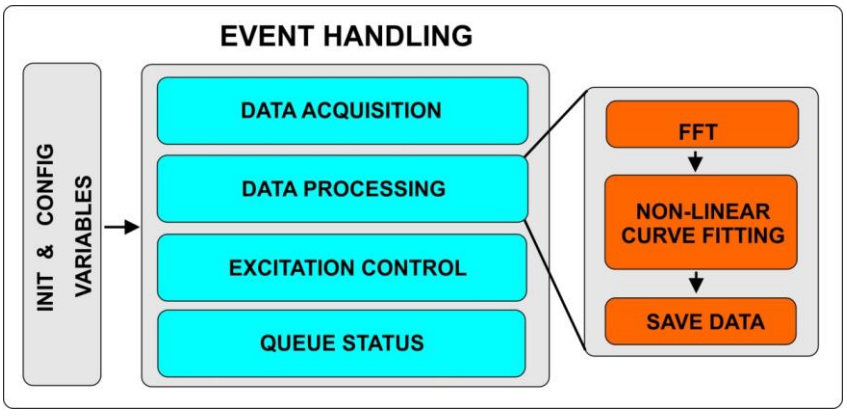

b)

Fig. 4–14. a) Graphical user interface developed in LabView for online tracking of the resonant frequency of HMB devices. The amplitude, peak frequency, baseline and Q-factor are obtained using a non-linear fitting of the spectrum and b) architecture of the software based on an event handling methodology to effectively capture samples, actuate the resonators and, processing and storing data.

4.2.5 Noise analysis and responsivity of the experimental setup

4.2.5.1 Thermomechanical resonance measurement and noise analysis

The noise analysis of the optical readout system was based on the work proposed by Lee et al. [10]. To relate the minimum achievable displacement of the device to the measured electronic signal, the thermomechanical noise of the resonators was determined. The thermomechanical motion of a resonator in the frequency domain is given by [11],

$$S_{x,th}^{1/2}(\omega) = \left[\frac{4\omega_0 k_B T}{QM_{eff}} \frac{1}{(\omega_0^2 - \omega^2)^2 + (\omega_0\omega/Q)^2}\right] \quad \text{Eq. 4.2}$$

The expression can be simplified when the resonator is on resonance,

$$S_{x,th}^{1/2}(\omega) = \sqrt{\frac{4k_B TQ}{\omega_0^3 M_{eff}}} \quad \text{Eq. 4.3}$$

where ω_0, k_B, T, Q and M_{eff} are the angular resonance frequency, Boltzmann constant, temperature, quality factor and effective mass of the device. We calculated the noise spectral density of the thermomechanical displacement on resonance of a hollowed resonator made of polycrystalline silicon with dimensions of 20 µm × 270 µm × 6 µm ($w \times l \times h$) considering the measured resonance frequency (650 KHz), quality factor (692), temperature (300 K) and effective mass. For the fundamental mode of a simple doubly clamped beam, the effective mass is given by $M_{eff} = 0.735ltw\rho$, where $l * t * w$ are the beam dimensions and ρ is the mass density of the beam [12]. Considering the size of the resonator as well as its composition, the mass of the resonator was calculated by FEM simulations resulting in an approximate value of 17 ng. By substituting the estimated mass into the above equation, the effective mass was M_{eff} = 12.495 ng, and thus, the thermomechanical displacement noise spectral density was estimated using Eq. 4.3 to be $S_{x,th}^{1/2} = 0.116\ pm/\sqrt{Hz}$.

4.2.5.2 Michelson interferometer responsivity

The analysis of the Michelson interferometer was essential to determine the minimum achievable displacement of the structures in terms of the transduced voltage of the photodetector. As Fig. 4–9 shows, the laser beam reflecting from the sample surface interferes with the laser beam from the reference mirror. This produces a constructive or destructive interference depending on the phase difference between both signals. Upon interference, the intensity on the photodetector can be expressed as follows,

$$I_{PD} = I_{sample} + I_{ref} + 2\sqrt{I_{sample}I_{ref}}\cos(kz - 2k * u(t)) \quad \text{Eq. 4.4}$$

Here, I_{sample} and I_{ref} are the intensities of sample and reference reflections, respectively, k is the wavenumber, z is the path length difference travel by the signals and $u(t)$ is the time displacement function of the microbeam surface. From the above equation, the maximum and minimum intensities measured by the photoreceiver can be calculated in terms of the constructive and destructive interference of the signals, as follows,

$$I_{max} = I_{sample} + I_{ref} + 2\sqrt{I_{sample}I_{ref}} \quad \text{Eq. 4.5}$$

$$I_{min} = I_{sample} + I_{ref} - 2\sqrt{I_{sample}I_{ref}} \quad \text{Eq. 4.6}$$

The difference between the maximum and minimum intensity values is known as modulation depth, $M = I_{max} - I_{min} = 4\sqrt{I_{sample}I_{ref}}$. The responsivity of the Michelson configuration can be defined as the ratio of smallest intensity on the photodetector with respect to the minimum optical path length change derived from the smallest displacement of the beam surface, $\mathcal{R} = \partial I/\partial z$. In this sense, the maximum responsivity for the Michelson setup configuration is obtained when the slope of responsivity function ($\partial I/\partial z$) is maximum for values of "z" equal to odd multiples of $\lambda/4$, as expressed by the following equation,

$$\mathcal{R}_u^M = \frac{\partial I}{\partial z}\Big|_{z=\lambda/4} = 4k\sqrt{I_{sample}I_{ref}} = \frac{2\pi}{\lambda}M \quad \text{Eq. 4.7}$$

In our experiments, the path length difference of the arriving signals was adjusted until a maximum responsivity was obtained. Afterwards, the power was measured using a digital optical power meter (PM100D Thorlabs). For an HMB device with dimensions of 20 µm × 270 µm × 6 µm ($w \times l \times h$) the depicted power values for the reference signal and the reflected light beam from the sample surface were approximately 350 µW and 120 µW, respectively. For these measurements, the intensity values when using a photodetector responsivity of $\mathcal{R}_{PD} = 0.4\ A/W$ and a AC transimpedance gain of 40 V/mA were determined to be 1.92 V and 5.6 V, respectively. Hence the maximum responsivity for the Michelson setup was calculated using the above equation as,

$$\mathcal{R}_u^M = \frac{2\pi}{633\ nm}\sqrt{19.2\ V\ *\ 5.6\ V}\ = 130\ \mu V/pm$$

On the other hand, by assuming that the total noise power spectral density (PSD) is the sum of the noise of individual sources we have:

$$S_{v,total}^{1/2} = \left(S_{v,th}^{1/2} + S_{v,sys}^{1/2}\right)^{1/2} \quad \text{Eq. 4.8}$$

here $S_{v,sys}^{1/2}$ is the voltage noise floor of the measurement system that includes noise and spurious signals caused by different sources such as mechanical vibrations, dark current noise, shot noise, laser noise, aberrations and misalignments of the optical elements of the setup. However, the maximum contribution for systematic errors can be attributed to the noise equivalent power (NEP) introduced by the photodetector. The NEP quantifies the sensitivity of the photodetector; it expresses the minimum optical signal that can be detected. Therefore, a low NEP is advantageous to have low noise features in the output signal. According to the manufacturer specifications, the photoreceiver 1801 has a maximum NEP of 30 $pW/\sqrt{Hz}$ within a frequency bandwidth from 0 to 200 MHz; and thus, considering an amplification gain of 2.4×10^4 V/W, the NEP was determined to be $0.720\ \mu V/\sqrt{Hz}$ or in other terms $S_{v,sys}^{1/2} \approx 0.720\ \mu V/\sqrt{Hz}$.

Finally, to determine the total noise power spectral density ($S_{v,tot}^{1/2}$), it was necessary to translate the thermomechanical noise of the resonator ($S_{x,th}^{1/2}$) into the electronic domain by means of the displacement to voltage responsivity of the Michelson setup, such that:

$$S_{v,th}^{1/2} = \mathcal{R}_u^M * S_{x,th}^{1/2} \qquad \text{Eq. 4.9}$$

$$S_{v,th}^{1/2} = 130\ \mu V/pm * 0.116\ pm/\sqrt{Hz} = 15\ \mu V/\sqrt{Hz}$$

Hence, the total noise power spectral density obtained for this resonator was $S_{v,total}^{1/2} \approx 15.72\ \mu V/\sqrt{Hz}$

References

[1] S. H. Tan, N.-T. Nguyen, Y. C. Chua, and T. G. Kang, 'Oxygen plasma treatment for reducing hydrophobicity of a sealed polydimethylsiloxane microchannel', *Biomicrofluidics*, vol. 4, no. 3, 2010.

[2] V. Jokinen, P. Suvanto, and S. Franssila, 'Oxygen and nitrogen plasma hydrophilization and hydrophobic recovery of polymers', *Biomicrofluidics*, vol. 6, no. 1, p. 016501, 2012.

[3] R. W. R. L. Gajasinghe, S. U. Senveli, S. Rawal, A. Williams, A. Zheng, R. H. Datar, R. J. Cote, and O. Tigli, 'Experimental study of PDMS bonding to various substrates for monolithic microfluidic applications', *J. Micromechanics Microengineering*, vol. 24, no. 7, p. 075010, 2014.

[4] 'Microchemcom. Retrieved 8 March, 2012, from http://www.microchem.com/pdf/SU-82000DataSheet2000_5thru2015Ver4.pdf.

[5] C. S. Thompson and A. R. Abate, 'Adhesive-based bonding technique for PDMS microfluidic devices', *Lab. Chip*, vol. 13, no. 4, pp. 632–635, 2013.

[6] S. Satyanarayana, R. N. Karnik, and A. Majumdar, 'Stamp-and-stick room-temperature bonding technique for microdevices', *J. Microelectromechanical Syst.*, vol. 14, no. 2, pp. 392–399, 2005.

[7] C. F. Carlborg, T. Haraldsson, M. Cornaglia, G. Stemme, and W. van der Wijngaart, 'A High-Yield Process for 3-D Large-Scale Integrated Microfluidic Networks in PDMS', *J. Microelectromechanical Syst.*, vol. 19, no. 5, pp. 1050–1057, 2010.

[8] E. R. H. John M. Nichol, 'Displacement detection of silicon nanowires by polarization-enhanced fiber-optic interferometry', *Appl. Phys. Lett.*, no. 19, pp. 193110 – 193110–3, 2008.

[9] C. I. Enriquez-Flores, J. J. Gervacio-Arciniega, E. Cruz-Valeriano, P. de Urquijo-Ventura, B. J. Gutierrez-Salazar, and F. J. Espinoza-Beltran, 'Fast frequency sweeping in resonance-tracking SPM for high-resolution AFAM and PFM imaging', *Nanotechnology*, vol. 23, no. 49, p. 495705, 2012.

[10] J. Lee, Z. Wang, K. He, J. Shan, and P. X.-L. Feng, 'High Frequency MoS2 Nanomechanical Resonators', *ACS Nano*, vol. 7, no. 7, pp. 6086–6091, 2013.

[11] Cleland, A.N., *Foundations of Nanomechanics: from Solid-State Theory to Device Applications*. 2003.

[12] K. L. Ekinci, Y. T. Yang, and M. L. Roukes, 'Ultimate limits to inertial mass sensing based upon nanoelectromechanical systems', *J. Appl. Phys.*, vol. 95, no. 5, pp. 2682–2689, 2004.

Chapter 5 Results and discussion

5.1 Characterization of 1st generation of HMB devices

As previously discussed in the Fabrication Chapter, the optical inspection with SEM micrographs and microscope images of the first generation of resonators showed an undercut effect at both clamped supports in some devices. The overhang length was proportional to the over-etched material under the region delimited by the tilt angle, as shown in Fig. 5–1. As a result, this produced a coupling effect between the set of microbeams. It also should be noted that owing to the poor selectivity between the silicon nitride and the doped silicon oxide materials, the sacrificial layer still remained in the main composition of the microbeams. Under these assumptions, an important deviation of the initial vibrational modes of the system was expected. Henceforth, in this section, some of the devices of wafers 2, 3 and 8 were experimentally characterized to verify the response of the optical setup readout and also to analyse their spectral frequency response, vibration amplitude and Q-factor. Furthermore, in order to understand the governing physics of mechanically coupled resonators, FEM simulations were employed. The coupling strength and its relationship between the dimensions of the set of microbeams was investigated including parameters such as separation distance, tilt angle, width and height of the beams. Finally, looking at mass sensing applications, a net mass was added to one of the beams to study the shift of the vibration modes. It has been demonstrated that mechanically coupled resonators are promising tools for improving by orders of magnitude the sensitivity of the micromechanical mass detection compared to the conventional frequency shift strategy [1]–[4].

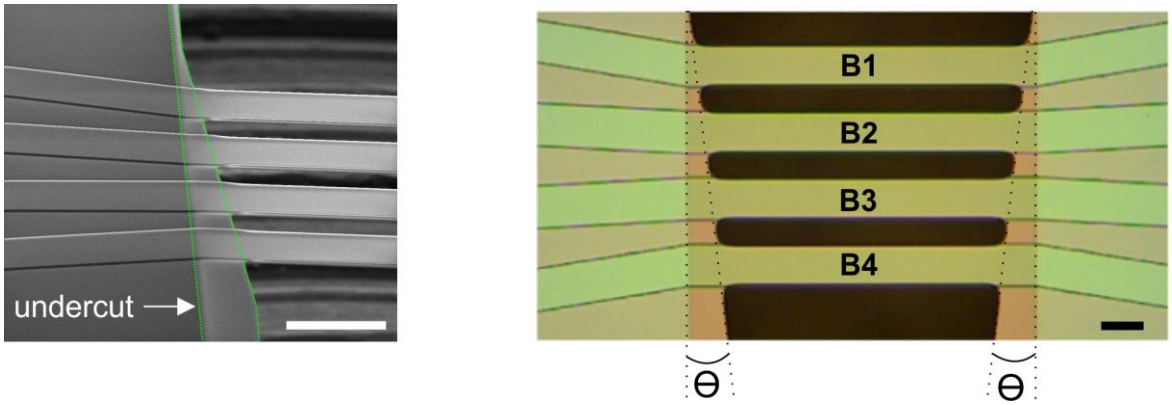

Fig. 5–1. Undercut effect presented in several HMB devices of the first generation because of the anisotropically overetching of the silicon-based substrate. The overhang length of the resulted coupled array of resonators is determined by the tilt angle outlined at both clamped supports. The elements of the array are numerically labelled in increasing order of the tilt angle. The scale bar on the SEM micrograph is 100 μm and on the microscope image is 35 μm.

5.1.1 Resonant frequency and Q-factor of uncoupled devices

For those devices from wafers 2, 3 and 8 that did not present an undercut effect, their frequency response was experimentally measured to analyse the effect of the material's properties, dimensions and energy dissipation of every resonator in the set of microbeams. There are two mainly differences among these wafers that should be considered during their experimental characterization. Wafers 2 and 3 have microbeams with height of 2 μm and LPCVD silicon nitride as based structural layer. Whereas the microbeams from wafer 8 have a depth of 5 μm with silicon nitride deposited by PECVD. To proceed, the thermal noise spectrum of the devices was characterized without any active actuation at room temperature and ambient pressure conditions using the experimental setup described in the previous Chapter. Unfortunately, not all the devices in a single wafer were eligible for experimental characterization due to the excessive residual stress of the silicon nitride structural layer that yielded material fracture and cracking of the resonators. Hence, we discussed the behaviour of some devices that maintained their integrity after the fabrication process. Fig. 5–2 shows the effect of the tilt angle over the spectral frequency response for a device with 35 μm width and pitch of 20 μm made of silicon nitride deposited by LPCVD. The exhibited frequency response of the set of microbeams was around 700 KHz with Q-factors of approximately 500. For this type of devices, the measured frequency response was 65% higher than the estimated by FEM simulations (around 250 KHz).

It is noteworthy that the exceeding residual stress in LPCVD silicon nitride resonators significantly caused an upward frequency shift in respect to the expected natural frequencies. Besides, the interplay between the tilt angle of the clamped supports and the center-to-center distance of the measured frequency peaks demonstrated a linear tendency: the higher the tilt angle, the greater the distance shown by the frequency peaks.

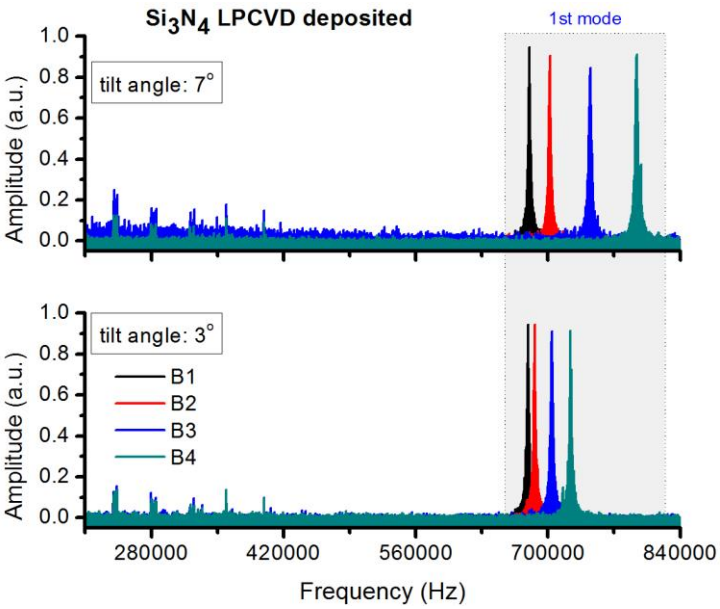

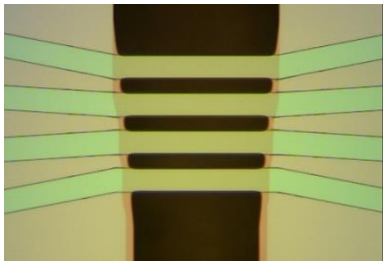

Fig. 5–2. Plots of the magnitude displacement *versus* frequency for an array of microbeams with 35 μm width and pitch of 20 μm made of LPCVD silicon nitride. The well distribution and localization of the frequency peaks indicates that the array of microbeams is not mechanically coupled. Devices with tilt angles of 7° displayed ample center-to-center distances between consecutive peaks. Inset shows a microscope image of the set of microbeams.

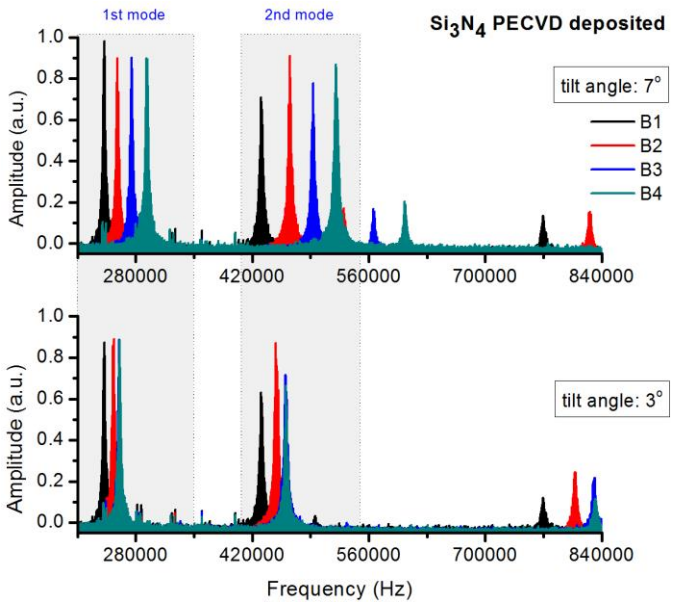

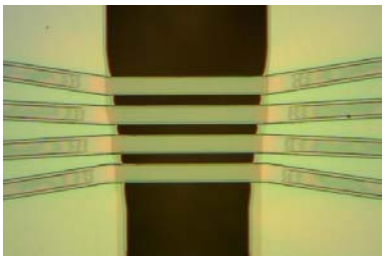

Fig. 5–3. Amplitude displacement for a set of microbeams with 35 μm width and pitch of 20 μm build by PECVD silicon nitride. The fundamental mode of the group of eigenfrequencies is around 250 KHz. The inset shows a partially etched structural material that caused a downshift frequency (65%) with respect to the expected frequency. The system is not mechanically coupled owing to the well outlining of the frequency spectrum amplitude of every microbeam.

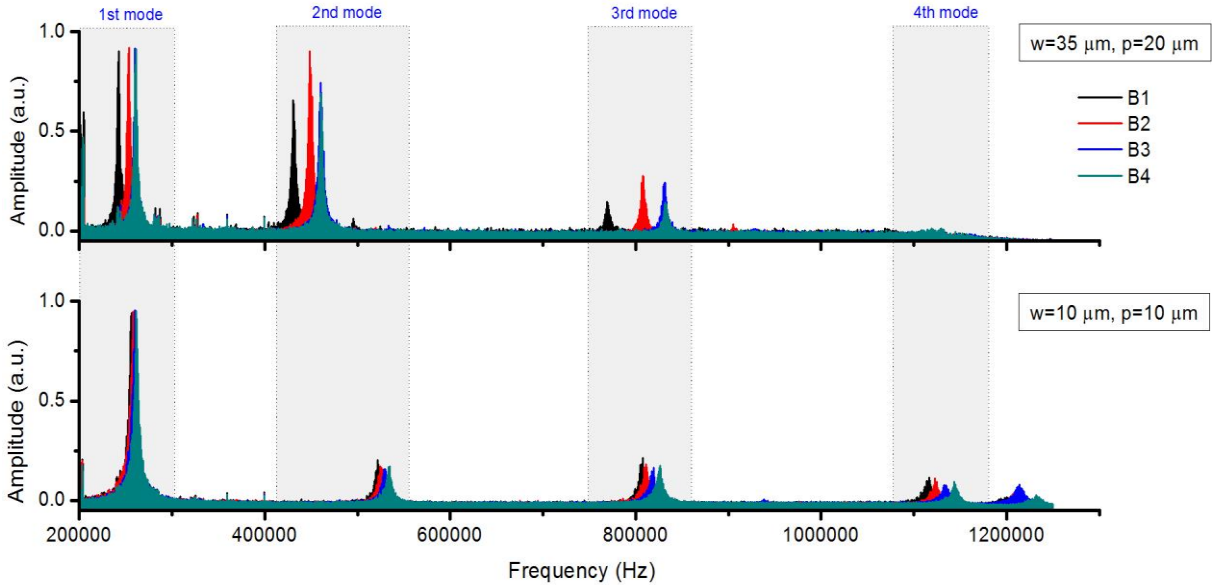

Fig. 5–4. A comparison of the non-mechanically coupled frequency response of devices made of PECVD silicon nitride with a tilt angle of 3°: a) for the narrower (w=10 µm) and more closely spaced microbeams (p=10 µm) and b) for the wider (w=35 µm) and more separated set of microbeams (p=20 µm).

The linear tendency was also verified for devices of wafer 8 along with a remarkable downward frequency (around 50%) shift with respect to the expected frequency response, as Fig. 5–3 shows. This can be explained because the devices fabricated by PECVD silicon nitride had a lower selectivity to the HF 49% acid etchant solution, and thus, during the sacrificial etching step, the structural layer was also partially etched reducing their initial dimensions. The modal analysis with FEM simulations confirmed that microbeams with a final depth of 2.5 µm displayed natural frequencies around 250 KHz, which is in good agreement with the experimentally measured ones. Furthermore, the optical readout could capture the response of the following fourth vibration modes of the set of microbeams owing to this downward frequency tendency. The response of higher-frequency modes indicated that the center-to-center peak frequency distance between the microbeams slightly increased in accordance to the mode number; in contrast to the displacement magnitude of the peaks that monotonically decreased, as depicted in Fig. 5–4. A comparison of the spectral frequency response of two devices from wafer 8 shows the influence of the width and pitch dimensions for devices with small tilt angles (3°). In general devices with smaller width and pitch dimensions showed frequency peaks more closely spaced with a reduced frequency bandwidth response and higher mean frequencies. On the other hand, the opposite effect was noticeable for devices with a tilt angle of 7° independently of the width and pitch dimensions of the array of microbeams.

5.1.2 Mechanically coupled devices

5.1.2.1 Theory

When a system is mechanically coupled, it will no longer display a single peak in the frequency domain, instead, it will exhibit localized vibration modes depending on the number of coupled elements and on the corresponding coupling strength between them. For instance, a pair of mechanically coupled microcantilevers by an overhang, which has been a coupled system studied by several authors [1], [5], can exhibit two localized vibration modes, as shown in Fig. 5–5. In the first localized vibration mode, namely symmetric mode, the pair of cantilevers is oscillating in phase along the out-of-plane direction. Whereas, in the second localized vibration mode, namely antisymmetric mode, the pair of cantilevers is oscillating out-of-phase.

Spletzer et. al [1] have indicated that the Anderson or localized vibration modes can be defined in terms of the amplitude displacement of the frequency peaks, thereby the system will become more localized when larger amplitude displacements are exhibited for a given eigenfrequency. If the magnitudes of displacement of the system are very similar but are not necessarily identical, then the localized vibration modes are said to be nonlocalized. On the other hand, DeMartini et. al [6] have outlined that a mechanically coupled system is highly localized when the vibration modes do not overlap, clearly differentiating the amplitude of vibration and ensuring ample separation of the frequency peaks. Also, the exhibited response of the system will be more similar to that of an uncoupled system showing more independent frequency peaks. From here and to avoid any confusion, the term "eigenstates" will be used to refer to the localized vibration modes of the system and indicate a different state of the displacement of the beams. Whereas for the characteristic frequency peaks of the system, the term "eigenfrequencies" will be employed.

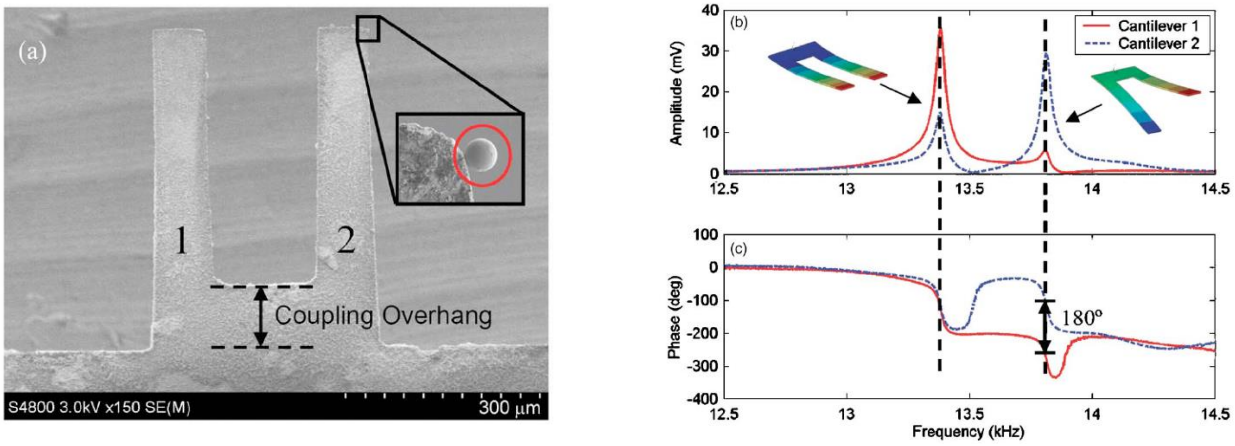

Fig. 5–5. SEM micrograph shows a system of two nearly identical microcantilevers mechanically coupled by an overhang. The resulted frequency response displays two eigenstates in which the structure is oscillating in phase (symmetric mode) and out-of-phase (asymmetric mode) [1].

Based on this assumption, if we consider an array of coupled resonators by an overhang with mistuned frequencies, the expected number of vibration modes will be directly proportional to the number of vibrating elements. Thus, the set of coupled microbeams from the first generation of HMB devices will exhibit four localized vibration modes in the frequency spectrum domain. This configuration can be considered originally in disordered in that all the resonators have different individual natural frequencies. However, initially disordered systems with nearly identical coupled subsystems, can advantageously have strong localized modes of vibration if the deviations of the individual natural frequencies are of the order of, or larger, than the coupling strength of the system [5]. Henceforth, by studying the nature of the coupling effect of our devices, we can understand and derive important implications in the enhancement of the amplitude sensitivity of the device for mass sensing applications along with the conventional resonance frequency shift approach.

5.1.2.2 Experimental response analysis

To illustrate the coupling effect of the first generation of HMB devices, Fig. 5–6 shows the frequency spectrum of an array of four coupled microbeams with 10 μm width, pitch of 10 μm and frame tilt of 7° obtained when the laser beam was focused onto the microbeam "B4". Each peak of the spectra, labelled in Fig. 5–6 from (A) to (D), corresponds to each of the first four eigenstates of the coupled system in which peaks with higher displacement amplitudes indicate that the energy of the vibrating system is concentrated in specific eigenstates. The modal analysis of the system indicates that the lowest resonance peak in the frequency spectrum (A) corresponds to an eigenstate where the microbeams move essentially together with the same phase similar to a single lumped mass. On the other hand, the modal analysis indicates that for higher-frequency peaks (B, C and D), one of the beams is oscillating out-of-phase with respect to the others. For these higher-frequency eigenstates the microbeam that is asymmetrically oscillating with respect to the others corresponds to the next lower beam wherein the localized mode is being displayed. Importantly, each of these resonance peaks oscillates at a slightly lower frequency (about 8% less) than the corresponding natural frequencies for the set of uncoupled microbeams.

The displacement amplitude, resonance frequency and coupling efficiency of each mode of the system depended on the specified dimensions of the microbeam configuration. The slightly variation in length of the microbeams ($Lb4 < Lb3 < Lb2 < Lb1$) introduced differences on their spring constants ($Kb4 < Kb3 < Kb2 < Kb1$). Hence, the coupling stiffness ratio was different between adjacent resonators ($\kappa = Kci/Kbi$) being lower for microbeams with smaller overhang length [5]. Regarding the disordered amplitude displacement of the coupled system, many factors can explain this behaviour. The real dimensions of the vibrating elements that integrate the resonating system can differ between each other due to manufacturing tolerances. Even the exhibited vibration amplitude of two symmetrically coupled cantilevers is initially not equal. Moreover, as these vibrating elements are highly susceptible to mass changes, any added mass to the cantilever surface can shift the resonance frequency and amplitude displacement of the resonators. In other words, it is expected that the amplitude of vibration of asymmetrically coupled microbeams was markedly different.

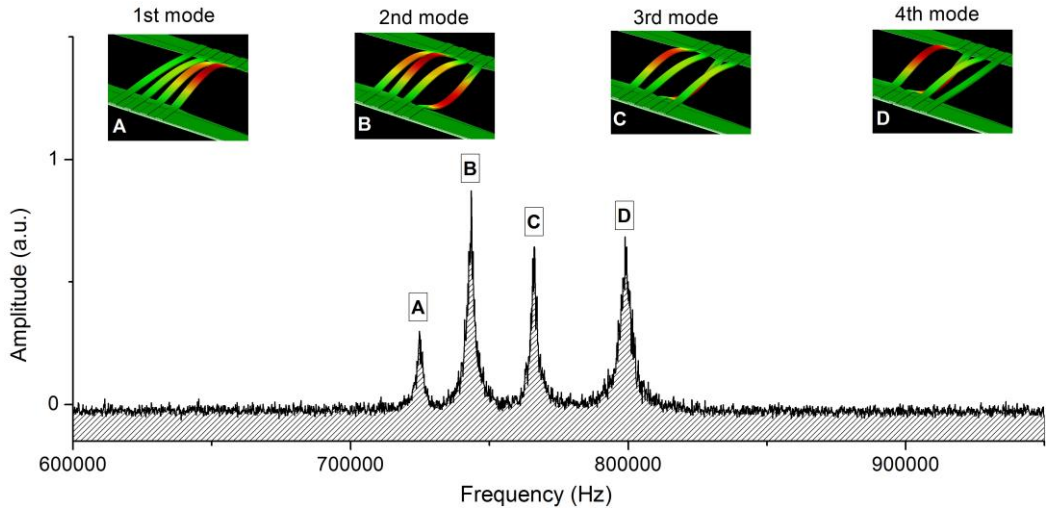

Fig. 5–6. Plot of the relative change in the eigenstates and their corresponding resonance peak frequencies for an asymmetrically coupled array of mistuned resonators. The insets display each of the first localized vibration modes of the coupled system obtained from the modal analysis with FEM simulations related to each eigenstate.

Since the asymmetrically array of mistuned resonators coupled by an overhand is a complex configuration to be modelled by a simple damped oscillator approach, the system was simulated in Comsol Multiphysics. With FEM simulations, forty-eight possible combinations were studied involving the most representative parameters that influenced on the coupling strength of the array of microbeams, as the width, gap distance and tilt angle. For carrying out the FEM simulations, the following assumptions were considered: i) silicon nitride was considered as the main structural material of the microbeams taking into account the still embedded doped silicon oxide sacrificial layer, ii) the model was implemented in the 3D domain taking into consideration the real dimensions of the beams based on the visual inspection with SEM micrographs and finally iii) the based-silicon substrate underneath both clamped supports had to be completely over-etched producing a well-defined overhang length, as Fig. 5–1 shows.

Basically the simulations consisted on two main tasks: an eigenfrequency study of the coupled system and a sweep frequency modal analysis when the system was driven on resonance by an external actuation force. In the latter one, the excitation signal was a sinusoidal wave with a frequency range spanned along the expected frequency bandwidth of the coupled system. Similarly to the actuation approach employed using a piezoceramic crystal beneath the chip to driven the response of the beams into resonance. Importantly, the residual stress of the fabricated devices was considered into the model by introducing an initial stress and strain condition along the longitudinal axis of the microbeams until the first set of natural frequencies matched the experimentally measured ones (about 700 KHz). The resulted prestressed value was 450 MPa. The eigenstates and eigenfrequencies calculated from FEM simulations for every modelled configuration of asymmetrically coupled microbeams are shown in Table 5-1 and Table 5-2. All the resulted eigenfrequencies were normalized with respect to the lowest found eigenfrequency (that was about 696190 Hz) to facilitate the comparison of results.

Table 5-1. Schematics of the eigenstates of an asymmetrically coupled array of four coupled microbeams of 10 µm width showing the interplay between the gap distance and tilt angle.

	Eigenstate 1	Eigenstate 2	Eigenstate 3	Eigenstate 4	
$tilt\ angle = 3^o$ $w = 10\ \mu m$ $p = 10\ \mu m$	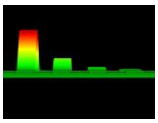	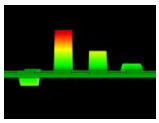	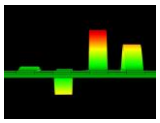	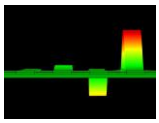	705980 Hz (1st eigenfrequency) BW = 6090 Hz
	1,41%	**1,63%**	**1,89%**	**2,28%**	
$tilt\ angle = 5^o$ $w = 10\ \mu m$ $p = 10\ \mu m$	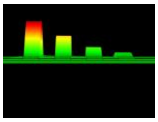	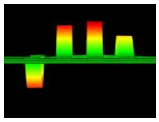	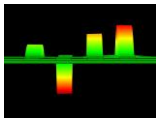	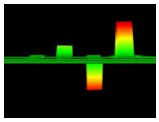	712340 Hz (1st eigenfrequency) BW = 19760 Hz
	2,32%	**2,97%**	**3,78%**	**5,16%**	
$tilt\ angle = 7^o$ $w = 10\ \mu m$ $p = 10\ \mu m$	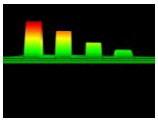	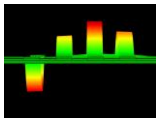	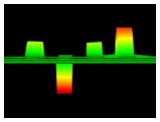	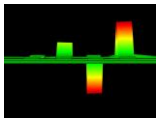	719800 Hz (1st eigenfrequency) BW = 40730 Hz
	3,39%	**4,72%**	**6,51%**	**9,24%**	

	Eigenstate 1	Eigenstate 2	Eigenstate 3	Eigenstate 4	
$tilt\ angle = 3^o$ $w = 10\ \mu m$ $p = 20\ \mu m$	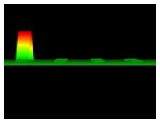	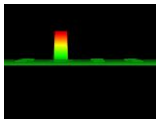	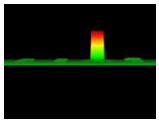	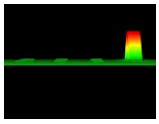	704980 Hz (1st eigenfrequency) BW = 7490 Hz
	1,26%	**1,58%**	**1,94%**	**2,34%**	
$tilt\ angle = 5^o$ $w = 10\ \mu m$ $p = 20\ \mu m$	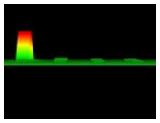	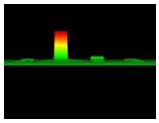	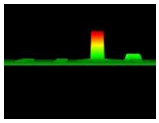	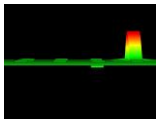	710620 Hz (1st eigenfrequency) BW = 17900 Hz
	2,07%	**2,79%**	**3,65%**	**4,64%**	
$tilt\ angle = 7^o$ $w = 10\ \mu m$ $p = 20\ \mu m$	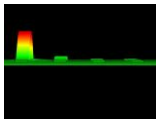	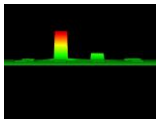	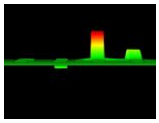	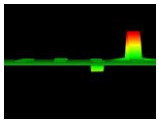	718000 Hz (1st eigenfrequency) BW = 32920 Hz
	3,13%	**4,42%**	**5,92%**	**7,86%**	

Table 5-2. Schematics of the eigenstates of an asymmetrically coupled array of four coupled microbeams of 35 μm width showing the interplay between the gap distance and tilt angle.

	Eigenstate 1	Eigenstate 2	Eigenstate 3	Eigenstate 4	
$tilt\ angle = 3^o$ $w = 35\ \mu m$ $p = 10\ \mu m$	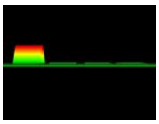	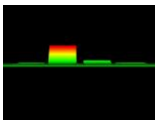	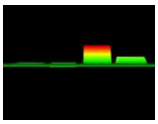	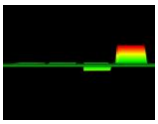	696500 Hz (1st eigenfrequency) BW = 4440 Hz
	0,04%	**0,19%**	**0,39%**	**0,68%**	
$tilt\ angle = 5^o$ $w = 35\ \mu m$ $p = 10\ \mu m$	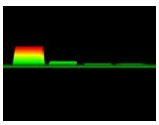	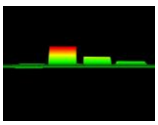	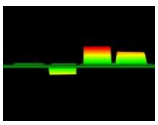	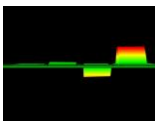	697990 Hz (1st eigenfrequency) BW = 13770 Hz
	0,26%	**0,64%**	**1,16%**	**2,24%**	
$tilt\ angle = 7^o$ $w = 35\ \mu m$ $p = 10\ \mu m$	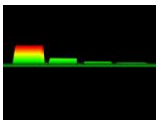	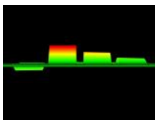	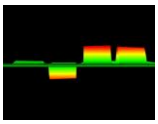	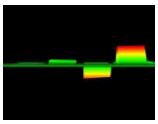	699870 Hz (1st eigenfrequency) BW = 29100 Hz
	0,53%	**1,22%**	**2,29%**	**4,71%**	

	Eigenstate 1	Eigenstate 2	Eigenstate 3	Eigenstate 4	
$tilt\ angle = 3^o$ $w = 35\ \mu m$ $p = 20\ \mu m$	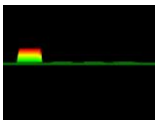	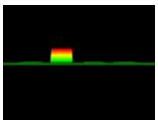	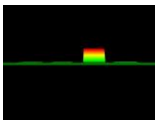	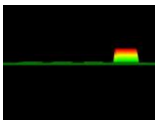	696190 Hz (1st eigenfrequency) BW = 4990 Hz
	0,00%	**0,17%**	**0,42%**	**0,72%**	
$tilt\ angle = 5^o$ $w = 35\ \mu m$ $p = 20\ \mu m$	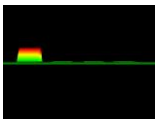	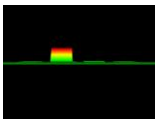	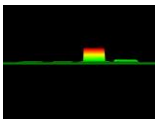	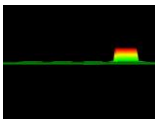	697180 Hz (1st eigenfrequency) BW = 12540 Hz
	0,14%	**0,55%**	**1,15%**	**1,94%**	
$tilt\ angle = 7^o$ $w = 35\ \mu m$ $p = 20\ \mu m$	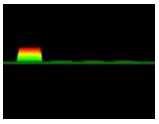	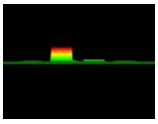	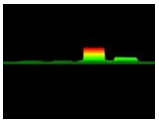	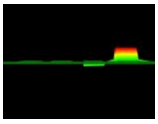	698570 Hz (1st eigenfrequency) BW = 23770 Hz
	0,34%	**1,08%**	**2,19%**	**3,76%**	

We experimentally interrogated the behaviour of some mechanically coupled devices from the first generation of HMB resonators and compared the results with the FEM simulations. The majority of the experimental measurements were focused on the response of the microbeam "B4" for the sake of simplicity, while performing the analysis and discussion of the various parameters involved.

Fig. 5–7a shows the direct interplay between the tilt angle and the evaluated frequency peaks for an array of coupled microbeam resonators. The amplification of this angle broadened the frequency bandwidth of the peak frequencies and increased their relatively center-to-center distances. Notably, the energy of the coupled system was distributed over the frequency spectrum as the overhang length increased, inducing a more localized response of the vibration modes. This trend was confirmed by the simulation results in which the definition of the eigenfrequency peaks was substantially improved for any of the measured configurations of coupled microbeams with higher tilt angles. Likewise, increasing the gap distance induced a more localized response of the vibrations modes of the system similar to the response displayed by an array of non-coupled devices (see Fig. 5–7b). This is because the exhibited frequency peaks show ample center-to-center distances facilitating the identification of each eigenstate. It rather seems that the measured eigenfrequencies were linearly shifted toward higher frequencies for greater gap distances. Unlike the response of two nearly coupled microcantilevers in which an exponential decay of the coupling constant has been observed as a function of their gap distance [5], the coupling constant of asymmetrically coupled microbeams turned out stronger as a function of increasing the pitch, which is comparable to the effect produced by the tilt angle inducing in sum a more localized behaviour.

Fig. 5–7c shows the results of the width and pitch variation of the microbeams dimensions over the displacements of the eigenstates for four configurations of coupled arrays of microbeams. The width of the microbeams directly influenced on the response of the set of peak frequencies causing an upward trend to higher frequencies for narrower microbeams due to the reduction of their effective masses. On the other hand, it is clearly seen that the downward frequency change of wider microbeams is then compensated by the effect of the gap distance increment. It also can be inferred that for wider microbeams, whose rigidity is larger, the coupling constant is less. In addition to this condition, when the gap distance was reduced to its minimum then the displayed eigenfrequencies overlapped. It is noticeable that those configurations of coupled microbeams that displayed overlapped eigenfrequency peaks showed an important reduction on their frequency bandwidth. For instance, the array of microbeams with 35 μm width, pitch of 10 μm and tilt angle of 3º, yielded the minimum frequency bandwidth of 4990 Hz (0.64%) with respect to the other configurations. The same effect was appreciable for narrow devices with similar dimensions (w=10 μm, p=10 μm, tilt angle=3º). In this case, the reduction of the microbeams width caused a relatively greater separation between the eigenfrequency peaks so that, when the tilt angle was change to 7°, the greatest frequency bandwidth was exhibited of approximately 40730 KHz (5.85%). Similarly, this particular configuration also displayed the maximum frequency shift of the first localized vibration mode of 760530 Hz (9.24%). In sum, the most representative parameters that induced a greater coupling effect were the gap distance and tilt angle, being the latter the one that most influenced on the coupling strength of the system. On one hand, the system is highly localized in terms of the frequency responses but is hard to say that is more sensitive with respect to the amplitude displacement of the localized modes. In this approach, a good indication that the system was highly localized was with respect to the ample separation between the frequency peaks.

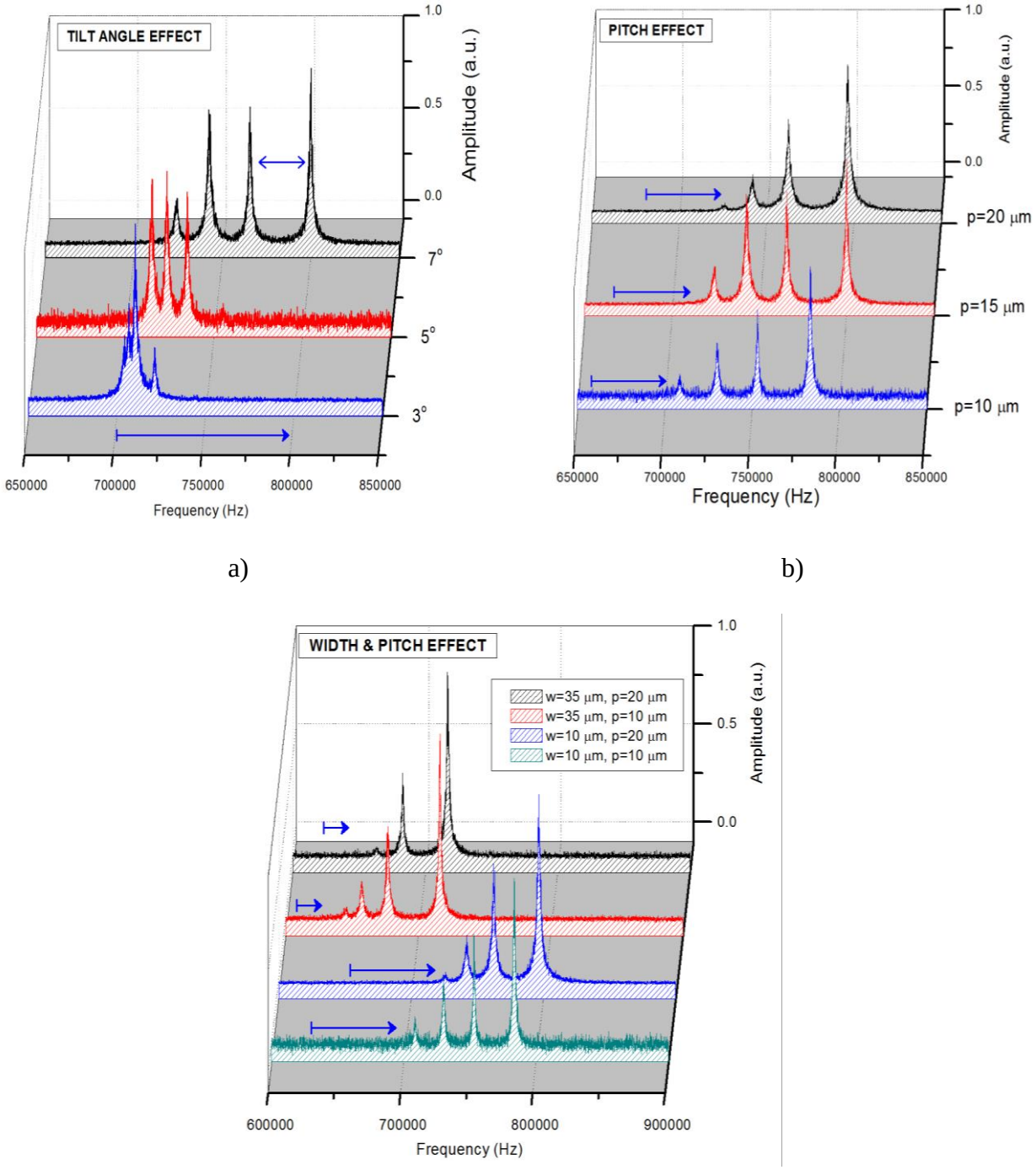

Fig. 5–7. Plots of the amplitude displacement *versus* frequency for different arrays of asymmetrically coupled resonators. a) Effect on the frequency response as a function of tilt angle at both clamped supports for microbeams of w = 10 μm and p =15 μm. b) Influence of the separation distance between microbeams with same width (10 μm) and tilt angle (7) over the displayed eigenstates of the system. c) Behaviour of the eigenstates with respect to various width and pitch dimensions of the microbeams for four configurations of coupled arrays.

From the experimental evaluations it was noticeable that the vibration amplitude of each eigenstate depended on the microbeam midspan where the laser beam was focused, as Fig. 5–8 shows. Although the overall eigenfrequency responses of the system could be acquired while focusing any of the microbeams, the amplitude displacement of the vibration modes was notably affected. Likewise, when the maximum amplitude of displacement of a given eigenstate of the coupled system matched with the measured microbeam, such as the 4th eigenstate when focusing onto the microbeam "B4", it can be inferred that the vibration mode was highly localized under these conditions. The dependence on the focused microbeam also produced that some eigenstates practically vanished or were not possible to be measure from the frequency domain such was the case of the 4th eigenstate when focusing on “B1” as shown in Fig. 5–8.

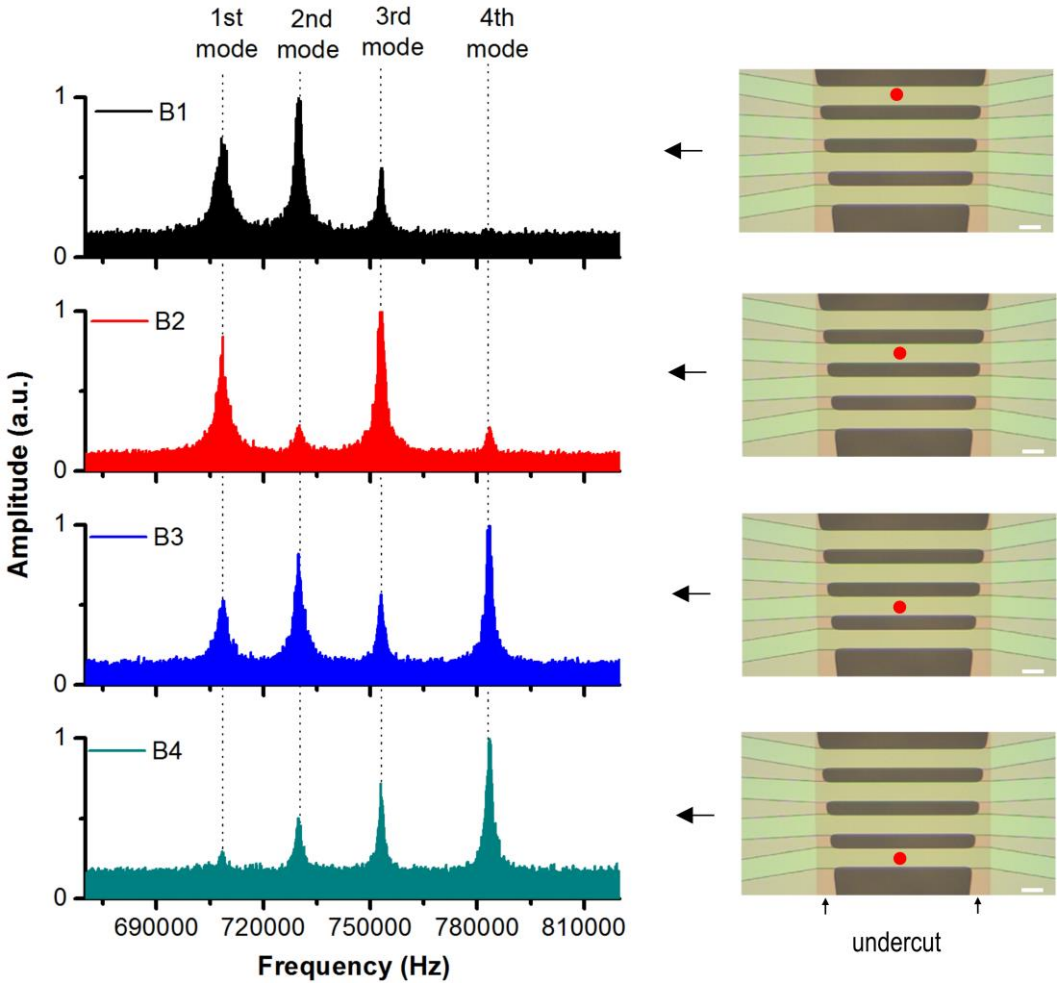

Fig. 5–8. Position dependence of the displacement amplitude of the eigenstates of a coupled system of four microbeam resonators with w=10 μm, p=10 μm and tilt angle of 7º with respect to the focused microbeam. The maximum amplitude of vibration is independent of the measured microbeam and is highly influenced by the energy distribution of the system.

From the modal analysis with FEM simulations, the driven response of each microbeam was acquired taking into account their corresponding position in the coupled array. In this way, we studied the behaviour of the eigenstates of the system according to the position of the microbeams as it was experimentally evaluated by the optical readout. The simulation results confirmed this interdependence but with some differences. For the majority of simulated configurations of coupled microbeams, the magnitude of displacement of the eigenstates did match with the correspondingly measured microbeam, as Fig. 5–9 and Fig. 5–10 show. This can be explained in terms of the study conditions used in the simulation environment to acquire the response of the eigenstates. To analyse the modal frequency response of the coupled system, the simulation study drives the response of the array of resonators into resonance by a frequency sweep along the frequency bandwidth of the system. As a result, the response of localized vibration modes can be undermined because the driving force is in-phase with each of the microbeams [7] in the same way as it happens when a vibrating system is piezoelectrically excited. By experimentally measuring the thermomechanical fluctuations of the coupled system, we ensured that the response of the system was spatially uncorrelated [5] allowing the acquisition of all the eigenstates.

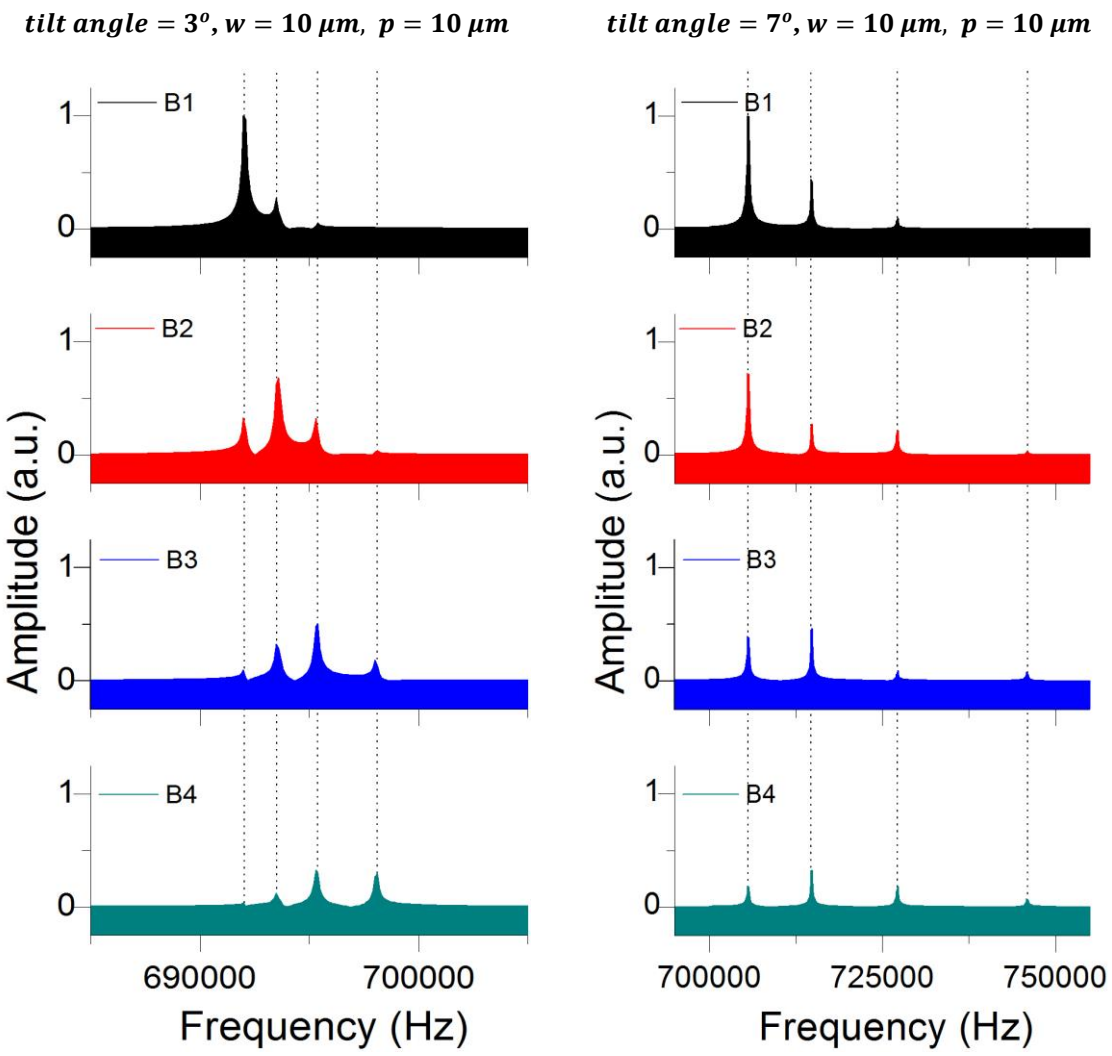

Fig. 5–9. Plots of the driven amplitude displacement *versus* frequency of the eigenstates of an array of four coupled microbeams obtained with FEM simulations. a) For small tilt angles the coupling constant decreases along with the frequency bandwidth and b) for higher tilt angles the frequency bandwidth is wider, showing well-spaced peaks that are shifted toward higher order frequencies.

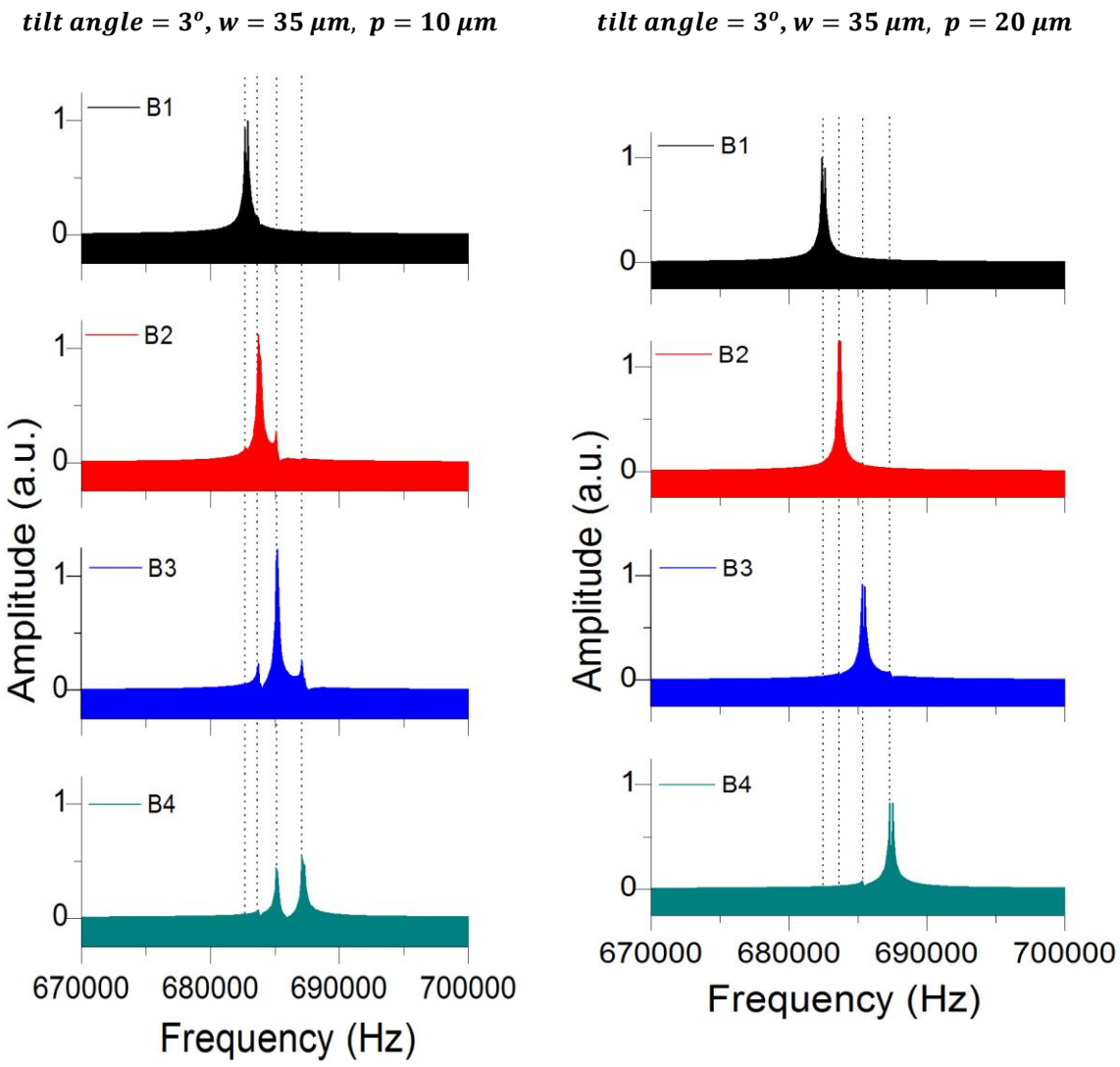

a) b)

Fig. 5–10. Plots of the driven amplitude displacement *versus* frequency of the eigenstates of an array of four coupled microbeams obtained with FEM simulations. a) For small tilt angles, wider microbeams overlapped their resonance frequency peaks leading to an important reduction in the frequency bandwidth and b) increasing the gap distance of wider microbeams with small tilt angles induces a notably downward shift of the set of frequency peaks (minimum reported eigenfrequency of 695190 Hz).

5.1.2.3 Added mass effect on coupled devices

To experimentally evaluate the effect of mass change over a mechanically coupled structure, a device made of LPCVD silicon nitride composed by microbeams with 10 μm width, pitch of 10 μm and tilt angle of 3° was employed. The added mass effect was investigated using the "dip and dry" approach, by which the resonance frequency is evaluated before and after exposing the device to the interrogated sample. In this way, a drop of Listeria solution 10 nM (in SSC 5x buffer) was deposited onto one of the microbeams (B4) by means of an inkjet deposition system (NanoEnabler system, Bioforce). Before performing the measurements, the drop was let to dry and care was taken to avoid contamination of the resonators.

Before the net mass was added onto the resonator "B4", the asymmetrically coupled set of resonators displayed well-defined eigenstates with ample eigenfrequencies when directly focusing on either of the microbeams midspan. However, when focusing onto the microbeam "B1", the 4^{th} eigenstate could not be captured because the maximum amplitude of displacement of the system was concentrated over the two first eigenstates. It can be said that the system was initially oscillating in disorder in that the exhibited displacement amplitude of every eigenstate was remarkably different indicating that the system was already localized. Adding a net mass onto one to the resonator caused a perturbation of the eigenstates and thus an energy redistribution of the system. Experimentally, this was confirmed by measuring the vibration modes of the system focusing the laser spot onto each of the microbeams, as Fig. 5–11a shows. In this way, we will present a discussion of the added mass effect concentrating on two main parameters: the displacement amplitude and the frequency shift of the set of microbeams.

Regarding the amplitude displacement of the eigenstates, apparently the perturbed system still remained in disorder. Since the amplitude of vibration of the eigenstates was unevenly distributed, then the energy of the coupled system was again confined in specific eigenstates. As depicted in Fig. 5–11b, when focusing on B1, the energy distribution of the system was concentrated on the 2^{th} and 3^{th} eigenstates with the largest displacement on the 2^{th} mode. Importantly, the most appreciable change in the effect of the added mass occurred in the 4^{th} eigenstate that initially was not noticeable in the previous eigenstate. When focusing on B2, the maximum exhibited amplitude displacement was on the 3^{rd} eigenstate indicating a shift of the energy distribution of the system toward higher-order frequencies. This effect was also depicted when focusing on B3 in which the 4^{th} vibration mode showed the maximum energy concentration of the system with the largest amplitude displacement (0.84 a.u.). Interestingly, the energy distribution of the system was more evenly distributed along the 4^{th} eigenstate when focusing on B4 respect to the initial state, with a subtle energy distribution tailored to the first two eigenstates. This behaviour is more similar to the response of an uncoupled system that displays ample eigenfrequencies and localized eigenstates. Therefore, it can be implied that measuring the response of the system onto the microbeam where the added mass was deposited, yielded the most localized vibration modes in contrast to the measured response on the other microbeams.

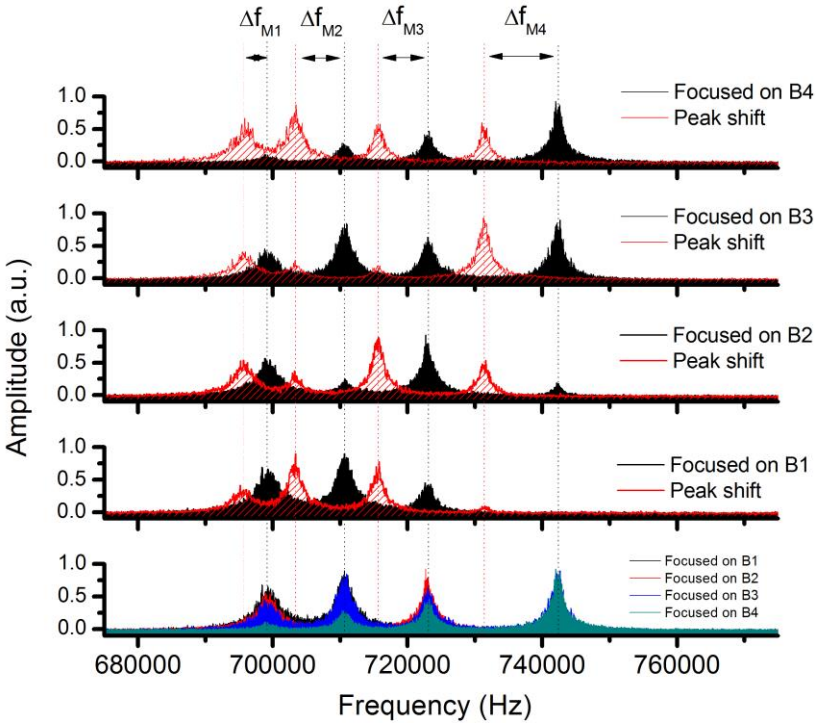

a)

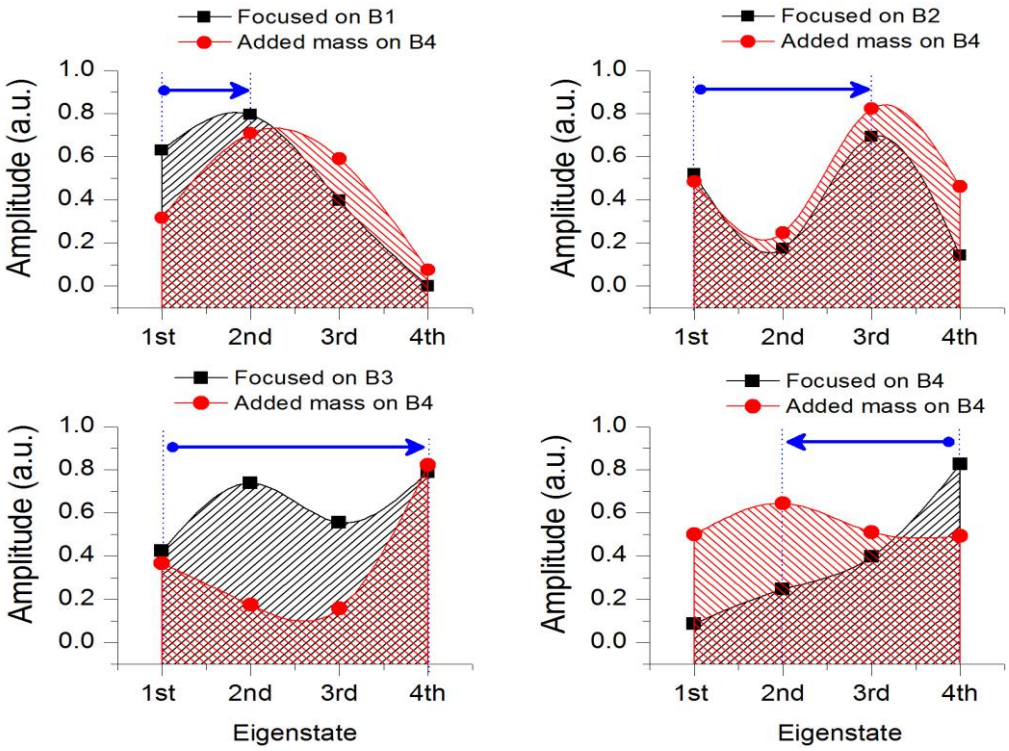

b)

Fig. 5–11. a) Effect of a net added mass onto microbeam "B4" over the eigenstates of a coupled array of microbeams with 10 μm width, pitch of 10 μm and tilt angle of 3°. The frequency response is acquired focusing the laser beam onto each microbeam, and b) analysis of the amplitude displacement of each eigenstate prior and after the added mass.

In sum, it can be said that the energy distribution of the system, when consecutively focusing the set of beams in ascending order (from B1 to B4), is similar to a sea wave that is travelling towards the shore and when finally reaches it, reinitializes its movement from back to forth, as Fig. 5–11b indicates.

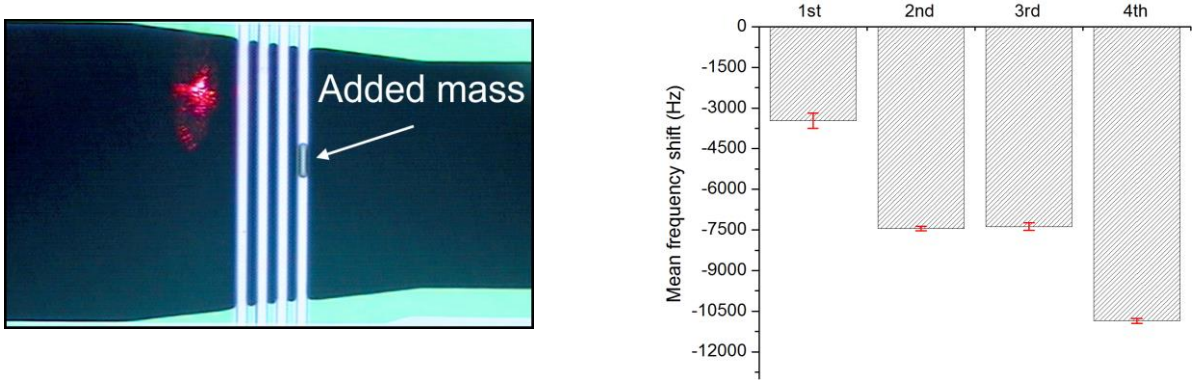

a) b)

Fig. 5–12. a) A microscope image illustrates the deposition of Listeria solution onto the microbeam "B4" to study the perturbation of the coupled array of microbeams. b) Frequency shift of the resonance peaks after adding the net mass in which the coupled system turns out to be more localized on the 4th vibration mode.

Another parameter that confirmed that the system became more localized after adding a net mass was the frequency shift of each eigenfrequency, as Fig. 5–12b shows. The highest frequency shift was exhibited by the 4th vibration mode (10.8 KHz) as expected because of the added mass over this microbeam. Similarly, the 2th and 3rd vibration modes showed downward frequency shifts with lower changes in comparison to the 4th eigenstate and with relatively closed frequency deviations (7.44 KHz and 7.38 KHz, respectively). Finally, the less localized vibration mode was the 1st eigenfrequency in which the resulted frequency shift was 3.65 KHz. In sum, the relatively frequency displacements after changing the effective mass of the system showed another pathway to verify that the system became more localized. This behaviour was also exhibited by a configuration of doubly clamped beams coupled to a lumped mass in which the highest frequency deviation was exhibited by the highest eigenstate [6].

5.2 Characterization of 2nd generation of HMB devices

5.2.1 Filling of embedded microchannels

The filling capabilities of HMB devices of the second generation with successfully integrated polymer microfluidic were investigated before the characterization of the density and viscosity of fluidic samples. Owing to the reduced amount of functional devices after the fabrication process, this preliminary filling study was limited to those arrays of microchannels whose composition and topology still remained.

Measurements of the contact angle of water with the surface of these devices at various locations and on several chips demonstrated a hydrophobic trend with an average contact angle of about 85º ± 5º. On one hand, this hydrophobicity level of the surface of the microchannels along with the hydrophobicity of the PDMS polymer were advantageous for cleaning purposes since the fluidic samples contained in the bypass microchannels were easily repelled from the sidewalls in a similar way as do PEEK tubes when transporting fluids into microfluidic systems. On the other hand, the visual inspection of the inner walls of the microchannels with SEM micrographs demonstrated a more planar and smoother surface as shown in Fig. 5–13a. Although the contact angle inside the cavities was not possible to be evaluated, it can be implied that this condition improved the filling capabilities and thus the injection of liquids.

The procedure for filling the arrays of HMB devices is detailed as follows. Water was pumped through one of the bypass channels at a constant flow rate (commonly at 10 µL/min) whilst the other bypass channel was let at ambient pressure as Fig. 5–13b shows. The required applied pressure to properly fill the microchannels depended on the initial flow rate and on the intrinsic resistance of the bypass channel, as it was studied by the FEM simulations. The intrinsic resistance of the bypass channel was the parameter that most influenced on the filling task which was adjusted by partially blocking its outlet or extending its length by connecting a long external tube with smaller cross section dimension. Besides, another parameter that influenced on the filling time of the microcavities was the physical properties of the liquid samples. For example, liquids with lower surface tension, as ethanol, more easily filled the microchannels by capillary forces. Furthermore, for those devices that presented difficulties to be filled, the ethanol solution aided to reduce their initial fluidic resistance facilitating the further injection of other liquids once the inner sidewalls were wetted.

Fig. 5–13c illustrates the filling process for an array of microchannels 35 µm width and with gap distance of 10 µm. Due to the greater dimensions of the cross section of these microchannels, water could more easily flow along the cavities but notably the process was not simultaneous. When the water meniscus reached the fluidic inlets of the microchannels, water did not immediately enter into the cavities. Instead, the larger dimensions of the inlet microchannels were used as reservoirs momentarily containing the water. Once all the fluidic entrances were wetted, the filling process started on the two middle microchannels, as Fig. 5–13c indicates. After a few milliseconds, the outer microchannels in the array were also filled. In contrast to the simulation results where transporting of water occurred in a sequential order, the experimental results demonstrated that the

filling process was not influenced by the position of the microchannels along the bypass channels. And notably, that the filling capabilities of the microchannels depended on the size of their cross-section.

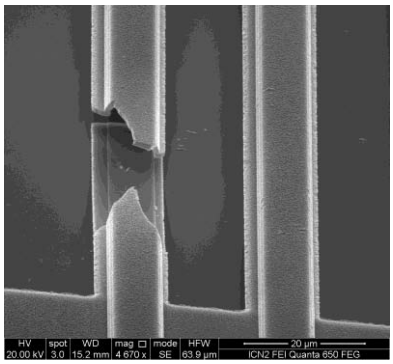

a)

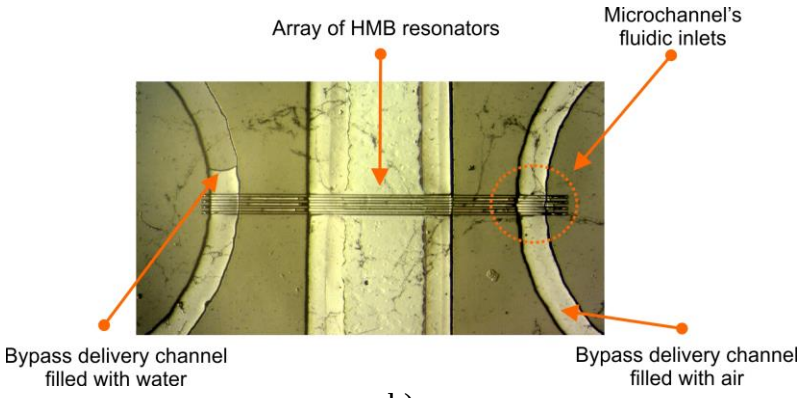

b)

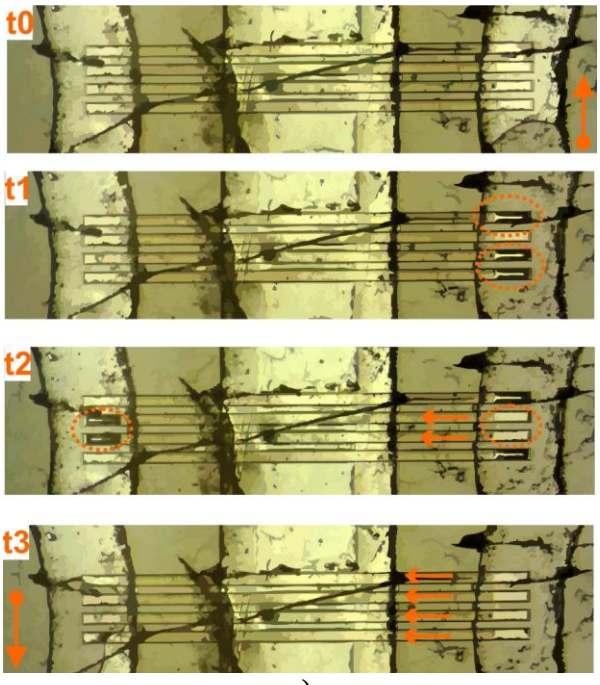

c)

Fig. 5–13. a) SEM micrographs illustrating the aspect of the inner walls of the microchannels. In contrast to the top structural layer of polysilicon, the appearance of this inner surface of the sidewalls is smoother. b) Microscope image of the filling process of an array of thin microchannels using a H-shape fluid delivery configuration. c) Filling process for microchannels of 35 µm width captured at various time frames.

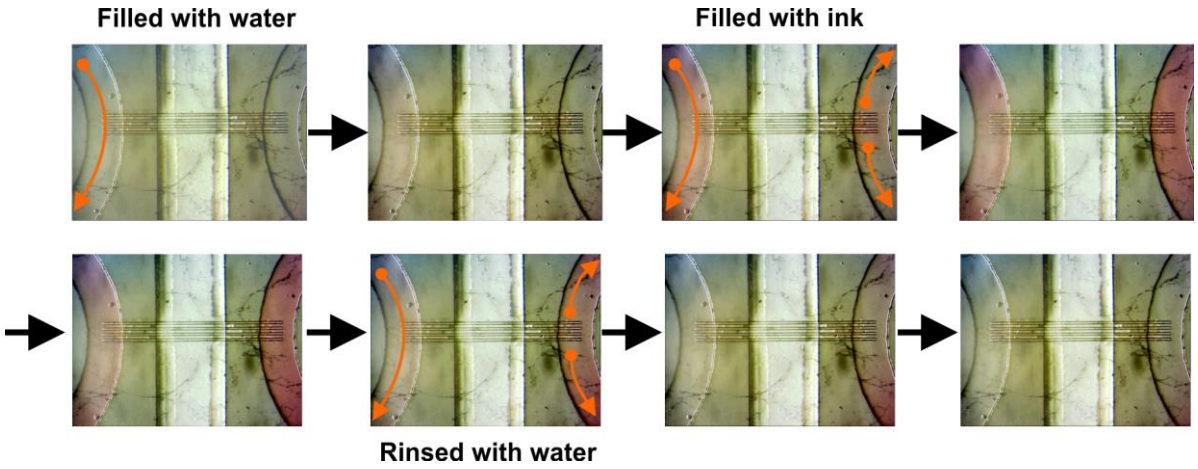

a)

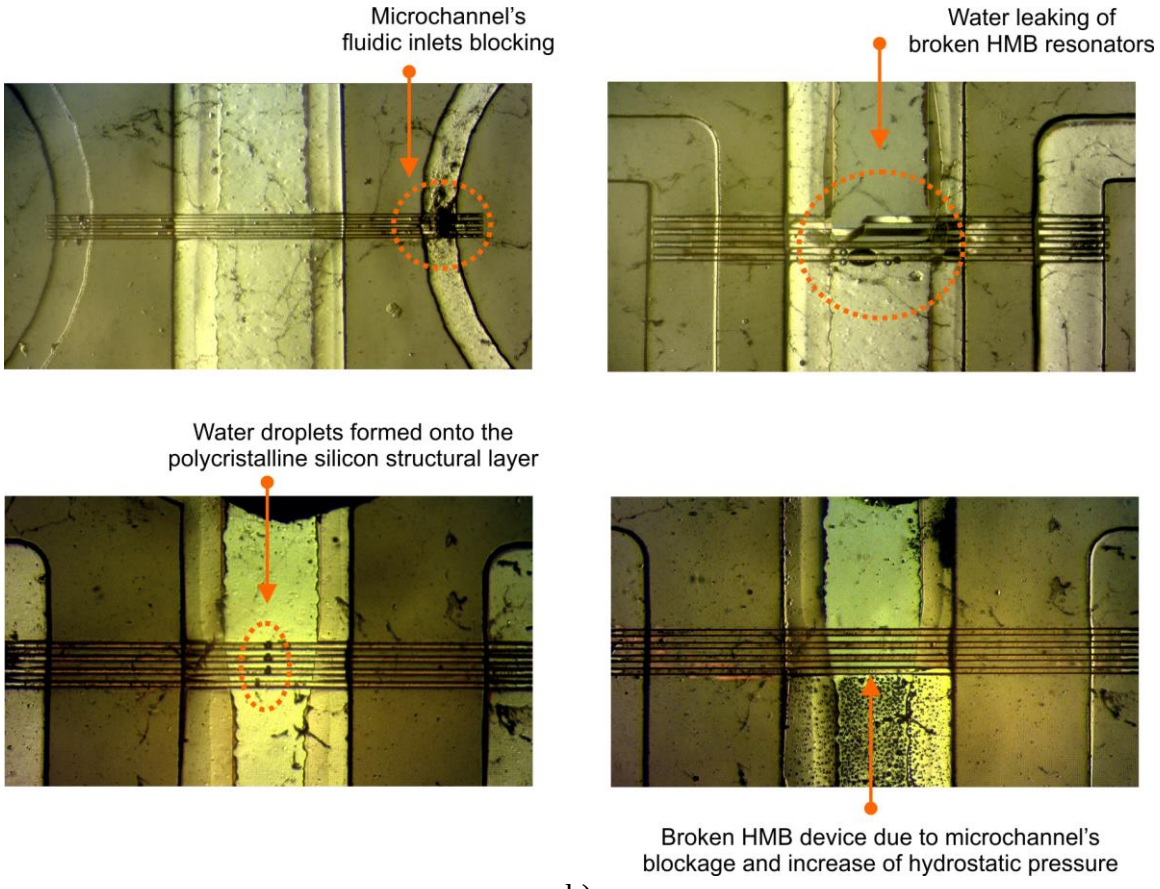

b)

Fig. 5–14. a) Photos that indicate the step by step process of exchanging fluids inside the array of the microchannels with *pink ink* and water from the left to right bypass channel. b) During the filling experiments the most common drawbacks presented included: the blocking of the inlet bypass channel, the leaking of water though broken resonators and the exceeding pressures that yielded fracture of the structural material using an in-line fluidic configuration.

Although the intrinsic fluidic resistance between microchannels with equal dimensions might differ from one microchannel to another due to microfabrication tolerances, once the microchannels were already filled, the exchange of fluidic samples inside the cavities was more easily accomplished as Fig. 5–14a illustrates. To overcome some of the drawbacks observed during the initial filling of HMB devices, a more precise control of the inlet hydrostatic pressure might facilitate the injection of fluids instead on directly relying on the initial flow rate or on the intrinsic resistance of the microchannels. Finally, Fig. 5–14b illustrates some of the problems that hindered the suitable transporting of fluids inside the microchannels.

5.2.2 Resonant frequency and Q-factor

By considering polysilicon as structural material with density of 2331 kg/m^3 and Young Modulus of 160 GPa [8], the analytical and FEM calculations showed that the expected fundamental resonance frequency of resonators of the second generation of HMB devices was approximately 918 KHz when filled with air. Instead, resonators showed a resonance frequency close to 650 KHz ± 10 Hz with Q-factor values of 692.23 ± 10 Hz operating at 23ºC and atmospheric pressure conditions as shown in Fig. 5–15a. The frequency variation was attributed to a modification on the effective length of the structures while releasing them from the substrate with HF 49% acid during the fabrication process. By an optical characterization with microscope images, we measured a lateral over-etching distance of approximately 25 µm, which modified the final effective length of each beam. These measurements correspond to an array of four embedded microfluidic channels of 1300 µm in length, cross-sectional area of 20 µm x 4 µm with a gap distance of 15 µm and tilt angle of 3°. The following analysis is presented for this HMB device due to the reduced amount of functional devices after the manufacturing.

The over-etching of the underlying sacrificial layer produced two main variations on the frequency response of the system. First, it decreased the overall frequency response of the resonators, but did not introduce a coupling effect on the system at all. To confirm this behaviour, Fig. 5–15a shows the time evolution of the sequential frequency response of the array of HMB resonators in air being "B1" the longest resonator and "B4" the shortest one. The optical characterization of the sensor response was performed by directly focusing on each of the middle point of the beam resonators. Notably, each frequency response is clearly differentiated for every resonator with and upward tendency for those devices with shorter effective length (B4). Particularly, the frequency variation between the resonators "B3" and "B4" is more closely unfolded which can be attributed to the subtle effect of the tilt angle. The second variation introduced by the over-etching effect was noticeable between the gap distances of the frequency peaks. From the FEM simulations, the expected gap distance for the same array configuration of HMB devices was 40 KHz in air. However, the experimentally measured separation distance is two order of magnitudes lower (0.4 KHz) than the expected. When comparing these results with the same configuration of HMB devices with coupling conditions, the separation distance between the localized vibration modes is also more widely distributed (about 20 KHz). In conclusion, an isotropic wet etching of the

underlying layer can be useful to modify the frequency response of HMB devices whenever the design of more closely spaced frequency peaks is necessary.

After characterizing the resonators in unfilled state, we studied the sensor performance when filled with water. The array of beams exhibited a frequency response close to 502 KHz$\pm$11 Hz with Q-factor values of 405.70$\pm$10, which represents a frequency shift of 148 KHz (22.77%) with respect to their response in air. As expected, the frequency shift was in accordance with the change in density of the fluid contained inside the microfluidic channels. Again, the frequency response for each resonator was clearly noticeable although the derived frequency shift was not proportional to every resonator. Fig. 5–15b illustrates the frequency shift when the array of beams was filled with water. The higher frequency shift variation was observed for the HMB device "B4" of about 23.2 KHz.

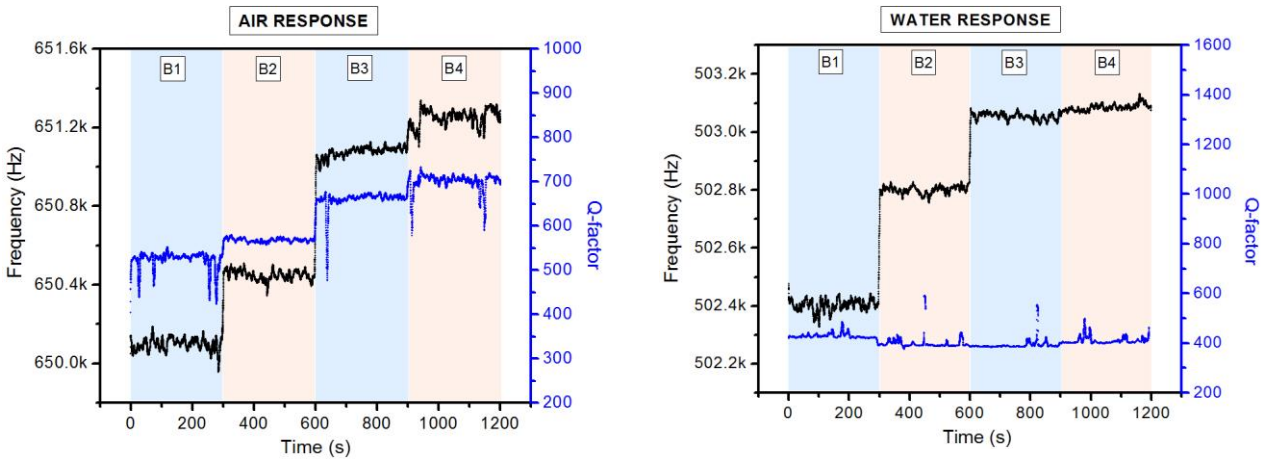

a) b)

Fig. 5–15. Plots of the time evolution of the frequency response of the array of HMB devices in the a) unfilled and b) filled state. The response is sequentially acquired by focusing on each middle point of the resonators for 5 min.

From here, the analysis of the HMB device was carried out focusing on the resonator "B4" which showed the best performance. Sensor noise was estimated based on measurements of the standard deviation of the frequency response of the resonator when filled with water, specifically when no frequency variation was expected ($\Delta f_R = 0$). Over a period of 45 min, the resonant frequency peak showed a standard deviation of $\sigma_R = \pm 10$ Hz. Although random sources of noise were involved in the acquisition system such as laser amplitude fluctuations and variations of the optical path of the interferometer when focusing onto the resonators, other sources of error could potentially be controlled. For example, increasing the number of acquired samples and reducing the excitation frequency bandwidth diminished systematic errors introduced by the Lorentzian curve fitting of the frequency response.

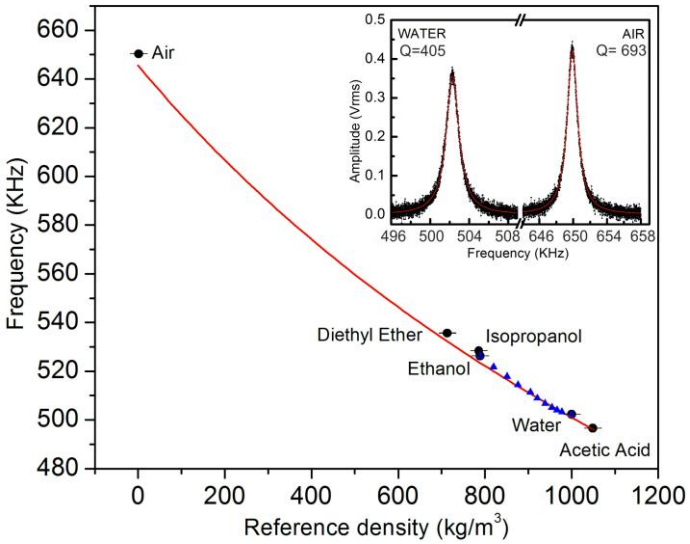

Fig. 5–16. Resonant frequency response of the resonator "B4" when filled with different solutions with well-known densities including water/ethanol mixtures. Inset shows the peak frequency response of the resonator before and after filling it with water showing a frequency shift of 148 KHz with a 41.1% quality factor decay. Error bars are smaller than black dots and represent a standard deviation of $\pm$10 Hz.

Thereafter, to calculate the mass responsivity of the HMB device, we used four samples with different and well-known densities (from Sigma Aldrich): diethyl ether (713.4 kg/m^3), isopropanol (786 kg/m^3), ethanol (789 kg/m^3), and acetic acid (1049 kg/m^3). The latter one was chosen to measure the linear response of the sensor beyond the density of the reference liquid (water). Fig. 5–16 shows the frequency response of the sample solutions with respect to their reference density values. The results demonstrate a clear relationship between the resonant frequency peak shift and the sample solution density according to the proposed model from Eq. 2.17. To calculate the sensitivity of the sensor, a linear curve fitting of data within this range of densities was calculated to report a $S_A = 148.75$ Hz/kg m^{-3} according to the following equation,

$$f(\rho) = 647524.24 - 148.75\,\rho \qquad \text{Eq. 5.1}$$

Our findings demonstrate that a minimum resolvable density change of 0.068 kg/m3 is achieved for a frequency resolution of $\pm$10 Hz. Also, we obtained a mass responsivity of 7.4 Hz/pg by dividing the above sensitivity with respect to the volume of the embedded microchannel (~20 pL), which is greater than previous devices [9],[10] but is limited as compared to sensors whose effective mass is smaller [11], [12]. Finally, the limit of detection of the sensor was calculated as LOD = $3*\sigma_R/S_A$ to report a value of **201.7 µg/ml.**

To study the sensor performance as a rheology analyser, we prepared binary solutions of ethanol and water. We injected solutions of ethanol with concentrations in volume from 0% to 100% with increments of 10%. Besides, the density of ethanol/water mixtures was calculated with a commercial pycnometer (10 ml pycnometer, Brand) at a fixed temperature of 23ºC to evaluate the frequency response of the sensor as a function of the density of samples, as shown in Fig. 5–17a. The average frequency peak over a time period of 10 min for each ethanol concentration is depicted in Fig. 5–18a. As expected, the interplay between the frequency of the sensor and density is inversely proportional with respect to the content of water/ethanol mixtures. This tendency is also observed in comparison with other calibration protocols [13]. The linear curve fitting of frequency with respect to density within this range showed a slope of 121 $\mathrm{Hz/kg\,m^{-3}}$. As Fig. 5–18b shows, complete sample exchange inside the resonators took about 7 minutes for a 10 µL/min flow rate in the inlet bypass channel. We noted that this time could be reduced by controlling the inlet bypass channel inflow to diminish dilution effects of mixtures with the initial reference liquid (water) that was contained inside the resonators.

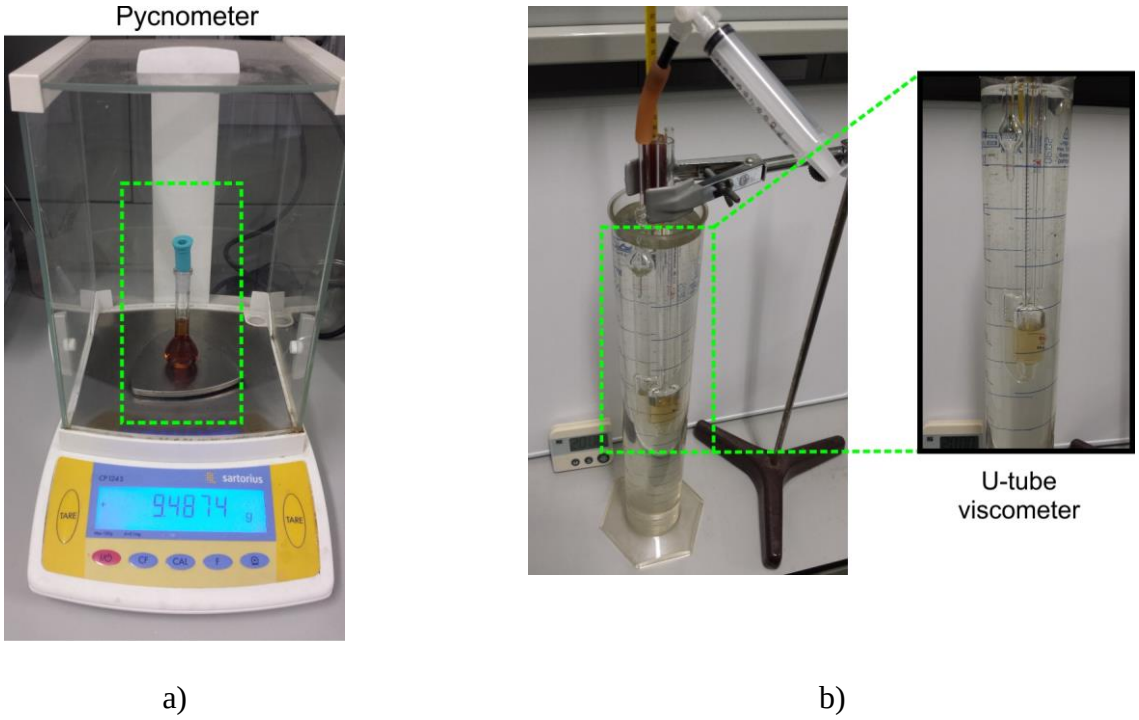

a) b)

Fig. 5–17. Mass density (a) and dynamic viscosity (b) measurements were performed with commercially available devices to compare the response the HMB resonators when characterizing different fluidic samples ranging from solvents, organic solutions and alcoholic drinks.

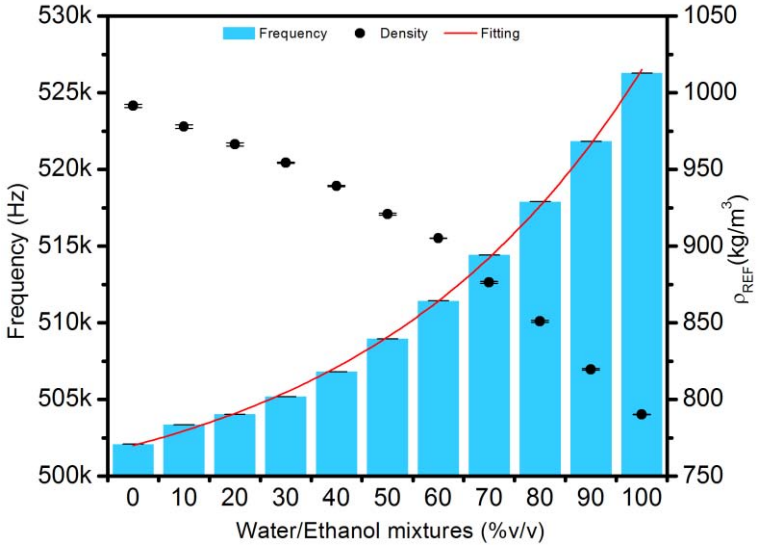

a)

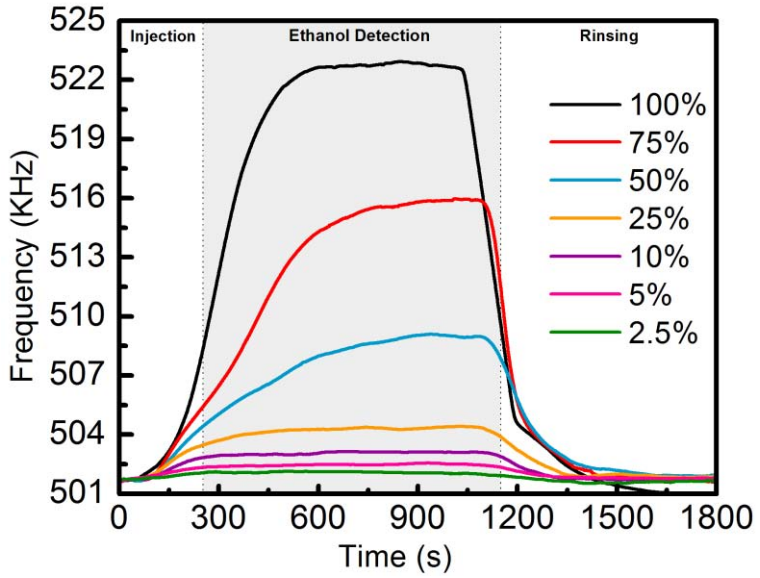

b)

Fig. 5–18. a) Resonant frequency response of a resonator with respect to binary mixtures of ethanol and water at different volumetric concentrations ranging from 0% to 100%. Data also shows the inversely proportional interplay of density values measured with a commercial pycnometer. b) Real-time evaluations of the shift in the resonant frequency to detect the minimum resolvable %v/v concentration. Dilution effects were noticeable during the first minutes of injection for higher ethanol concentrations.

Furthermore, the results demonstrate an increasing exponential trend in frequency as ethanol concentration increased while modifying the sample density according to the following curve fitting equation,

$$f(\%v/v) = 497178.74 + 4824.114\ \exp^{-0.01806(\%v/v)} \quad \text{Eq. 5.2}$$

From here, the minimum resolvable ethanol concentration of 0.115% was computed for a frequency resolution of $\sigma_R = \pm 10$ Hz. As follows, sensor Signal-to-Noise ratio (SNR) was calculated for the minimum ethanol concentration as $\Delta f_{2.5\%}/\sigma_R$; where $\Delta f_{2.5\%} = 418$ Hz is the frequency shift derived from a 2.5% ethanol concentration, yielding a SNR of 41.8, as shown in Fig. 5–18b.

As regards the energy dissipation of the sensor, the reported Q-factor value of resonators was 692.23 ± 10 when filled with air. Interestingly, the Q-factor also followed a linear tendency displaying higher values as a function of higher displayed frequencies with subtle variations ($\Delta Q \approx 60$) whereby the resonator "B4" displayed the maximum Q-factor (693) as Fig. 5–15a shows. This trend can be associated directly to the improvement in the frequency response of every resonator. However, after filling the microfluidic channels with water, the quality factor decreased to 405.70 ± 10 for all the resonators, which represents a decay of 41.1%. This effect is similar to another approach with SMR devices [14] when the contained liquid was replaced with water showing a 40% decay of the quality factor. To better understand this behaviour, we compared the response of the quality factor of the resonator "B4" when filled with binary mixtures of water/ethanol, with the corresponding dynamic viscosities. The viscosities were calculated with a commercial Ubbelohde viscometer (UBBEL02UKC, Sigma-Aldrich) at a fixed temperature of 23ºC, as Fig. 5–17b shows. Interestingly, the experimental results showed a decrease in the dissipation of energy of the resonator (enhancement of quality factor) as a function of increasing viscosity. This effect is contrary to the Q-factor response depicted by low stress silicon nitride SMR devices [10] in which the quality factor decreased as a function of increasing viscosity of water/ethanol mixtures. This can be explained in terms of the dimensionless frequency number by considering $h_{fluid} = 4\ \mu m$ and taking into account the values of density and viscosity calculated from the reference sensors. For instance, the value of β after filling the microchannel with ethanol was 31.81. Fig. 5–19a clearly shows that for our device, the computed values of β for water/ethanol mixtures are within the low inertia regime ($\beta < 46$). In this regime, since there is low inertia, the fluid follows the solid displacement of the resonator resembling a rigid-body oscillation. This explains the improvement in Q-factor values with increasing viscosity from 1 cP to 2.6 cP. From here, we correlated the Q-factor values of water/ethanol samples with respect to their reference viscosity values as shown in Fig. 5–19b, which resulted in a linear behaviour according to the following curve fitting approximation,

$$Q(\eta) = 325.78 + 82.5\,\eta \quad \text{Eq. 5.3}$$

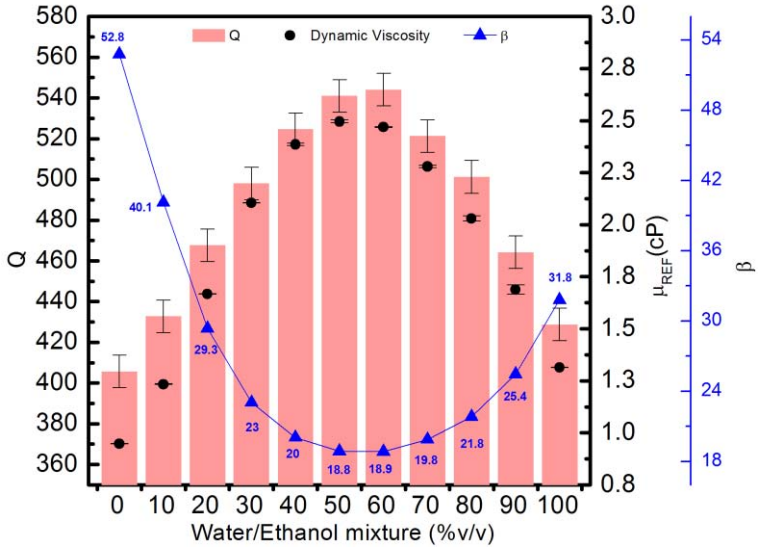

a)

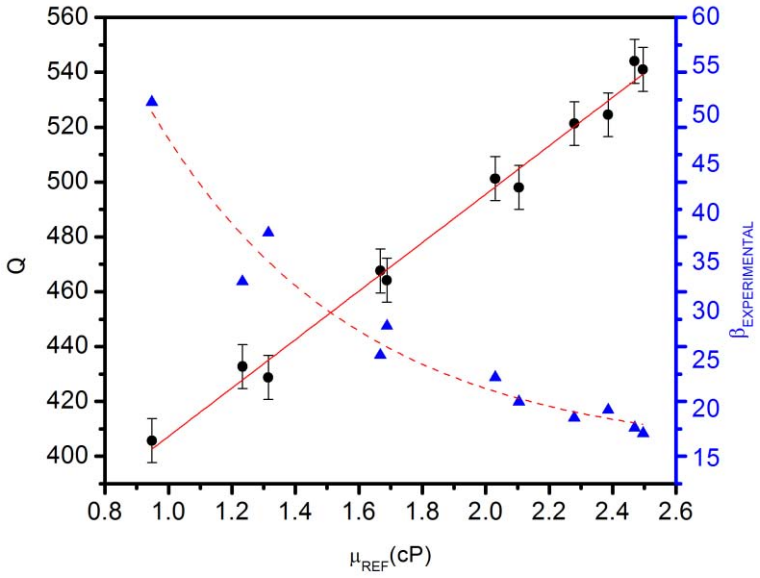

b)

Fig. 5–19. a) A linear tendency is depicted by the Q-factor values as the viscosity of the binary mixtures increases within the viscosity regime from 1 cP to 2.6 cP. b) The experimental values for ß demonstrate de interplay between fluid inertia and Q-factor values.

The minimum resolvable viscosity change of 0.15 cP was computed for a Q-factor resolution of ± 10. Experimentally, β decreased exponentially as a function of sample viscosity, which confirms the low inertia regime of the sensor, as Fig. 5–19b shows.

5.2.3 Density and viscosity evaluation of alcoholic drinks

Finally, we tested the device performance to measure the density and viscosity of a variety of alcoholic beverages on the resonator "B4". We compared four distilled beverages that contained no added sugar (spirits), and one distilled beverage with added sugar and flavourings. For the group of distilled alcoholic beverages there was a close correlation as density increased with a percentage error below 0.56%. In particular, beverages such as vodka, whisky and rum, which contain 40% ABV (alcohol by volume), depicted close frequency values among them with an average resonant frequency of 506.6 KHz ± 11 Hz, as Fig. 5–22 shows.

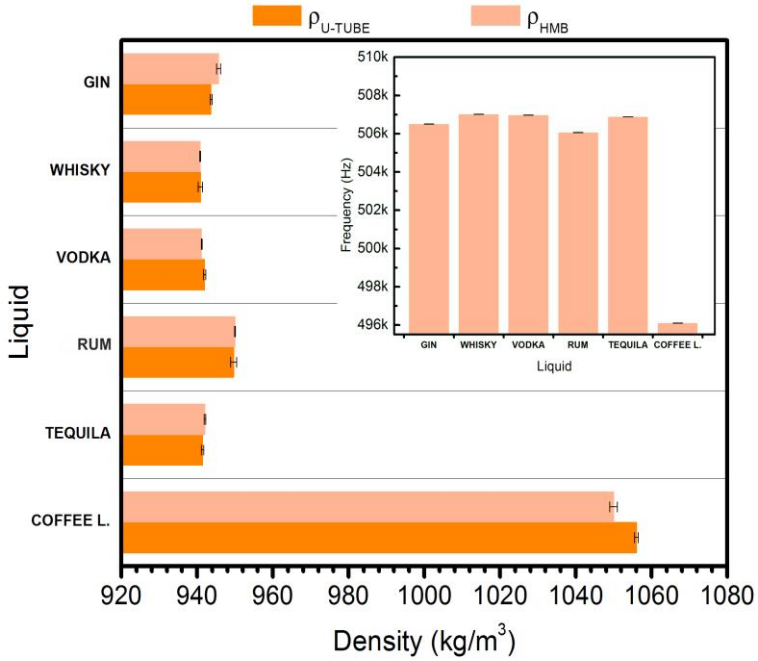

Fig. 5–20. Resonant frequency response of various alcoholic drinks confirms the inversely proportional relationship with their corresponding values in density.

However, measurements with coffee liquor exhibited a frequency response (496.105 KHz ± 11 Hz) below the reference liquid frequency, showing that sugar concentration and flavourings influenced on the density values more than the ethanol content. In comparison with hydrometers and pycnometers when used to determine the density of alcoholic drinks, the HMB resonator significantly reduced time per measurement to a few minutes and required lower sample volumes of only 250 µL. Afterwards, we calculated from Eq. 5.3 the dynamic viscosity of the alcoholic drinks, with a percentage error below 2%, by tracking the response of the quality factor of the sensor, see Fig. 5–21. Deviations from the expected value (7.67%) were observed for the coffee liquor beverage given that its dynamic viscosity is out of the linear viscosity regime of the sensor. Fig. 5–22 shows the feasibility to identify alcoholic drinks as a function of their corresponding values of density and viscosity.

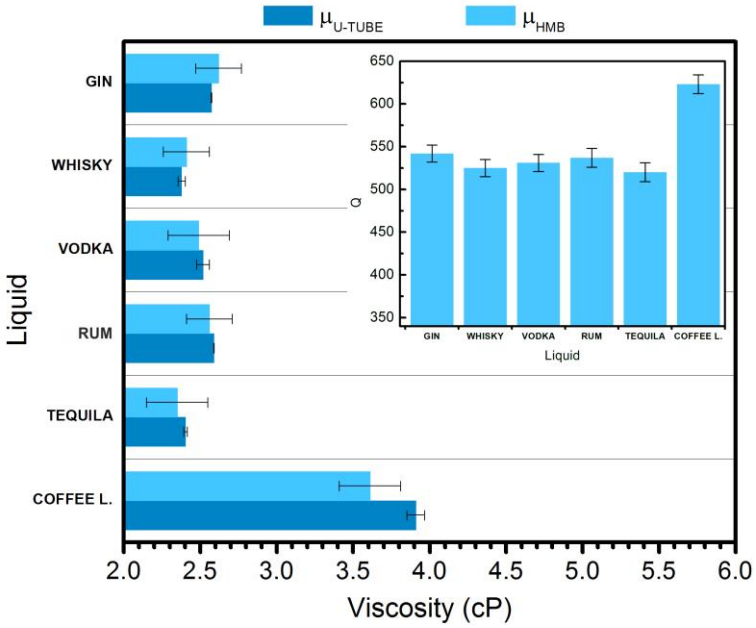

Fig. 5–21. Within the linear viscosity regime between 1 cP and 2.6 cP the viscosity of distilled alcoholic drinks can be calculated. The error increases for viscosities beyond 2.6 cP as is the case for the coffee liquor.

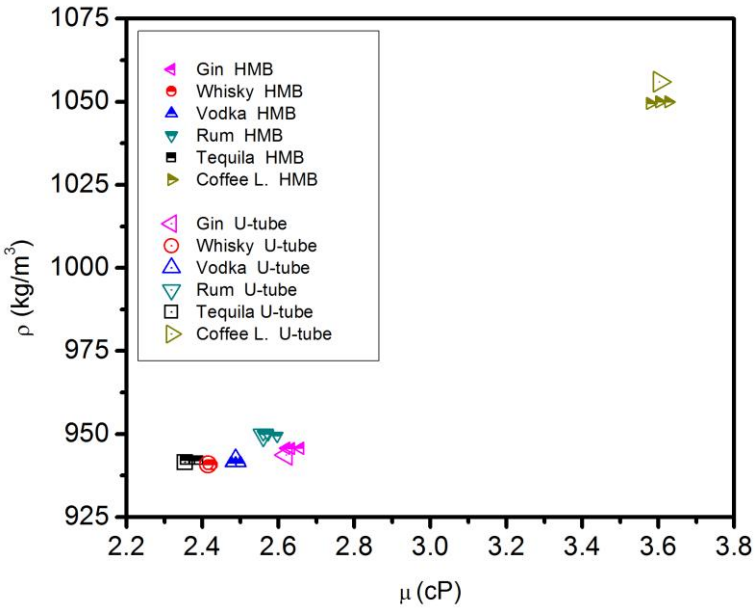

Fig. 5–22. Comparison of experimental values from the HMB sensor with respect to the values from reference sensors for identification of alcoholic drinks.

5.3 Characterization of 3rd generation of HMB devices

This section complies with the characterization of HMB devices of the third generation after their fabrication. Unfortunately, only a single device from wafer 4 was useful enough to determine the frequency response, to check the filling capabilities, the influence of a moderate vacuum and the possibility to achieve an efficient piezoceramic excitation due to the reduced fabrication yield of this generation of resonators. Fig. 5–23 shows the HMB device containing a microchannel with a cross-section of 16 µm and 4 µm of width and height, respectively.

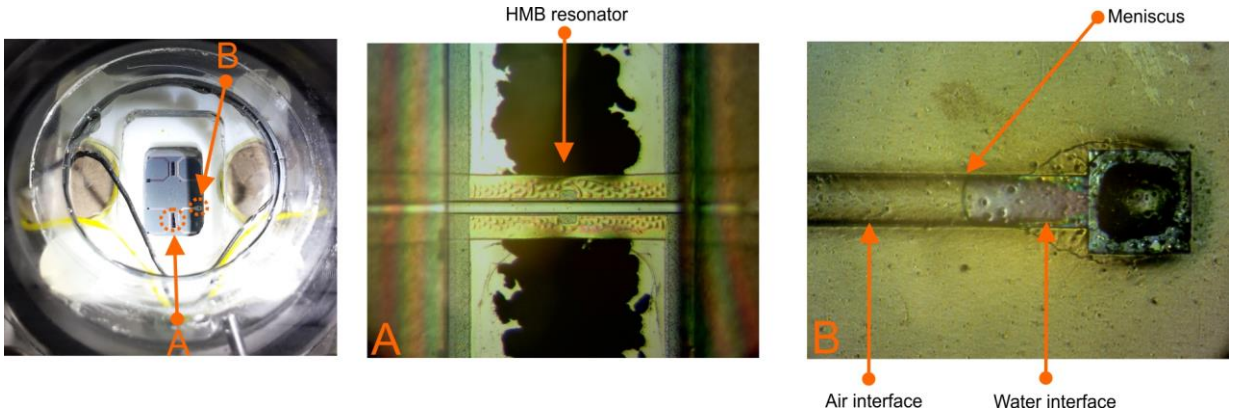

Fig. 5–23. Experimental characterization of a HMB resonator belonging to the third generation of devices using the holder support for actuation and air extraction. (A) Close view of a single HMB resonator. Traces of the structural material remained along the edges of the microchannels to correctly define the resonators. (B) Access through-hole of injection of liquids from beneath the chip. Water is pumped inside the microchannels through the right bypass channel.

In air, the driven resonant response of the HMB resonator displayed a frequency of 1.105 MHz ±11 Hz operating at 23ºC and moderate vacuum, as shown in Fig. 5–24. This value represents a 57% increase of the frequency response with respect to the 2nd generation of HMB devices in unfilled state. The frequency enhancement can be attributed to the effective length reduction of the resonator while releasing the doubly clamped structures from the based substrate. The visual inspection of the structure with microscope images verified a 75 µm overhang at each clamped support.

To characterize the device in the filled state, water was pumped through one of the bypass microchannels at a flow rate of 10 µL/min. Fig. 5–24 shows the time evolution of the frequency response of the resonator while its effective mass was shifted due to the contained liquid. The resulted frequency shift was 9.78 KHz which represents a magnitude of at least one order below than that exhibited by the 2nd generation of HMB devices. Despite the increase in frequency response of the resonator, it is remarkable that the sensitivity of the sensor was affected by the

added mass of the remaining structural material along the sidewalls of the microbeam. In consequence, the ratio of mass per unit length of the resonator was bigger than that of the fluid.

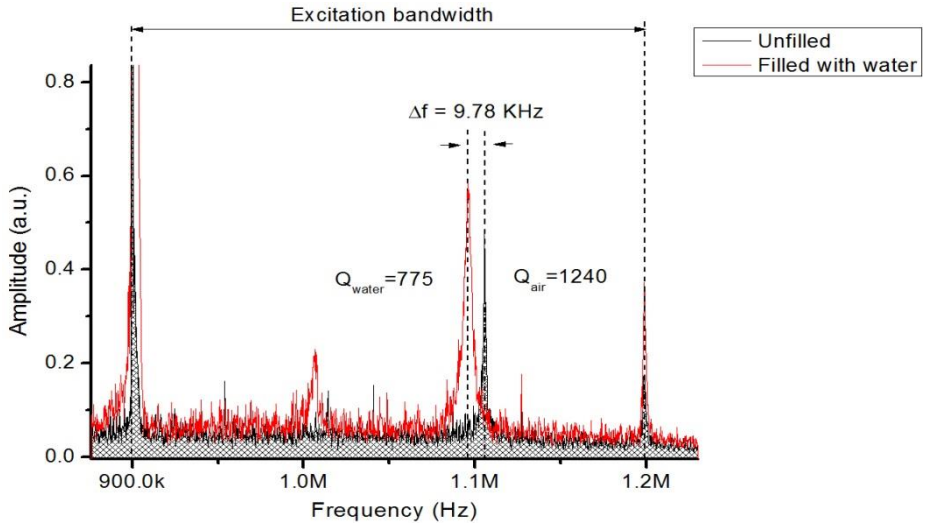

a)

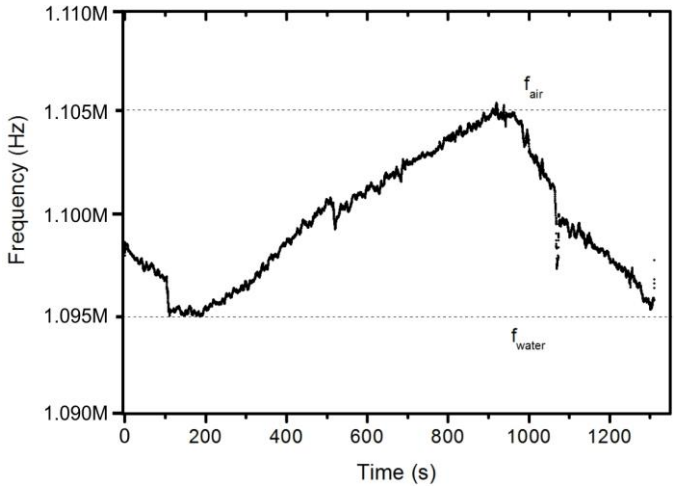

b)

Fig. 5–24. a) A higher resonance frequency is displayed by this generation of devices due to the effective length reduction of the resonator while releasing the microbeam from the based substrate. A better frequency bandwidth excitation was shown when two piezoceramic actuators were driven at 5 Vpp, clearly defining the frequency actuation window. b) Plot of the frequency response *versus* time while filling the microcavity with water.

The H-shaped filling configuration was useful to demonstrate the exchange of water inside the microchannels, as shown in Fig. 5–23. However, the total time required to completely exchange water inside the microchannels (t = 700 s) was twice the one needed for the previous generation of devices (300 s). Traces of protective resin could have partially blocked the entrance of the microchannel retarding the entire filling process.

Regarding the energy dissipation of the resonator, by applying a moderate vacuum, the Q-factor response markedly enhanced by 78% (1240) in comparison with the previous fabricated HMB devices. To maintain this behaviour, one of the major challenges was the suitable sealing of the microfluidic inlets of the bypass channels with the external tubing connections using the miniature O-rings. Water easily leaked out from the fluidic interconnections degrading the Q-factor response of the resonator. By applying an additional pressure to the upper plastic lid using the four bolts, the sealing improved, but the applied force was limited to prevent fracture of the device due to its reduced thickness (300 μm).

Fig. 5–24 demonstrates a decay of the Q-factor of 37.5% when the HMB device was filled with water which is in agreement with our previous design. Particularly this resonator behaved in the high inertia domain ($\beta = 123$) by considering the following parameters: $f_0 = 1.095$ MHz, $\rho = 1000$ kg/m^3 and $\eta = 0.894$ cP. Furthermore, the oxidation process of the microchannel walls improved the wettability of the third generation of HMB devices. Measurements of the contact angle (59.1° ± 0.26) at several locations on the surface of the chip indicated a more hydrophilic surface.

References

[1] M. Spletzer, A. Raman, A. Q. Wu, X. Xu, and R. Reifenberger, 'Ultrasensitive mass sensing using mode localization in coupled microcantilevers', *Appl. Phys. Lett.*, vol. 88, no. 25, p. 254102, 2006.

[2] B. E. DeMartini, J. F. Rhoads, M. A. Zielke, K. G. Owen, S. W. Shaw, and K. L. Turner, 'A single input-single output coupled microresonator array for the detection and identification of multiple analytes', *Appl. Phys. Lett.*, vol. 93, no. 5, p. 054102, 2008.

[3] M. S. Hajhashemi and B. Bahreyni, 'Characterization of Disturbances in Systems of Coupled Micro-Resonator Arrays', *IEEE Sens. J.*, vol. 12, no. 7, pp. 2510–2516, 2012.

[4] C. F. Reiche, J. Körner, B. Büchner, and T. Mühl, 'Introduction of a co-resonant detection concept for mechanical oscillation-based sensors', *Nanotechnology*, vol. 26, no. 33, p. 335501, 2015.

[5] E. Gil-Santos, D. Ramos, V. Pini, M. Calleja, and J. Tamayo, 'Exponential tuning of the coupling constant of coupled microcantilevers by modifying their separation', *Appl. Phys. Lett.*, vol. 98, no. 12, p. 123108, 2011.

[6] B. E. DeMartini, J. F. Rhoads, S. W. Shaw, and K. L. Turner, 'A single input–single output mass sensor based on a coupled array of microresonators', *Sens. Actuators Phys.*, vol. 137, no. 1, pp. 147–156, 2007.

[7] T. M. Huber, B. C. Abell, D. C. Mellema, M. Spletzer, and A. Raman, 'Mode-selective noncontact excitation of microcantilevers and microcantilever arrays in air using the ultrasound radiation force', *Appl. Phys. Lett.*, vol. 97, no. 21, p. 214101, 2010.

[8] S. D. Senturia, *Microsystem Design*. Springer US, 2005.

[9] J. Lee, R. Chunara, W. Shen, K. Payer, K. Babcock, T. P. Burg, and S. R. Manalis, 'Suspended microchannel resonators with piezoresistive sensors', *Lab Chip*, vol. 11, no. 4, pp. 645–651, 2010.

[10] M. F. Khan, S. Schmid, P. E. Larsen, Z. J. Davis, W. Yan, E. H. Stenby, and A. Boisen, 'Online measurement of mass density and viscosity of pL fluid samples with suspended microchannel resonator', *Sens. Actuators B Chem.*, vol. 185, pp. 456–461, 2013.

[11] V. Agache, G. Blanco-Gomez, F. Baleras, and P. Caillat, 'An embedded microchannel in a MEMS plate resonator for ultrasensitive mass sensing in liquid', *Lab. Chip*, vol. 11, no. 15, pp. 2598–2603, 2011.

[12] R. A. Barton, B. Ilic, S. S. Verbridge, B. R. Cipriany, J. M. Parpia, and H. G. Craighead, 'Fabrication of a Nanomechanical Mass Sensor Containing a Nanofluidic Channel', *Nano Lett*, vol. 10, no. 6, pp. 2058–2063, 2010.

[13] I. S. Khattab, F. Bandarkar, M. A. A. Fakhree, and A. Jouyban, 'Density, viscosity, and surface tension of water+ethanol mixtures from 293 to 323K', *Korean J. Chem. Eng.*, vol. 29, no. 6, pp. 812–817, 2012.

[14] T. P. Burg, J. E. Sader, and S. R. Manalis, 'Nonmonotonic Energy Dissipation in Microfluidic Resonators', *Phys. Rev. Lett.*, vol. 102, no. 22, p. 228103, 2009.

Chapter 6 Conclusions and Future Perspectives

Recent breakthroughs in the field of micro and nanoscale resonators with embedded microchannels have proven useful for a myriad of applications in engineering, chemistry, medicine and biology. This Doctoral Thesis followed this trend aiming to develop a new biosensor MEMS platform capable of performing simultaneous and multiple detection of analytes. The solution drawn up in this Thesis introduced a methodology wherein the fluidic samples were confined into an array of microfluidic beam resonators following two main directions: i) design, fabrication, and establishment of a robust technology and ii) by suggesting actuation and detection schemes of the MEMS sensors which can afford the acquisition of the response of more than a single resonator.

As a first step, we validated the governing physics and microfluidic behaviour of the proposed HMB devices employing analytical and FEM modelling. FEM simulations were not only a valuable tool for studying the structural mechanics, and estimating the mass responsivity and dynamic response of the resonators before their fabrication, but also for elucidating their performance based on the real dimensions of the final fabricated devices.

The work has encompassed a solid fabrication knowledge through the development of three manufacturing approaches of HMB devices using standard surface and bulk micromachining techniques at the Large Scale Facility (ICTS) of the IMB-CNM-CSIC. Designs were created following the criteria imposed by the analytical and FEM analysis and according to the availability and feasibility of the fabrication processes. However, batch processing of HMB devices resulted challenging at clean room facilities owing to the complexity of the technology and the high number of fabrication steps involved until completion which caused long leading times to demonstrate the operability of the devices. For these reasons, the work was constantly adapted based on the results of the manufacturing process by focusing on improving the technology of each generation of HMB devices from different perspectives and their applicability as mass sensors.

The first generation of HMB devices demonstrated the importance of a previous proper study and design before the fabrication process to select the right combinations of materials and fabrication steps. Although this approach was not capable of building hollowed resonators, it was useful for acquiring new insights for mass detection applications based on the behaviour of mechanically coupled systems. During the fabrication process, an under-etching effect introduced changes on the effective length of the structures and thus the microbeams were asymmetrically coupled by a small

overhand. The experimental characterization of these coupled HMB devices showed a direct interplay of the coupling strength of the system in respect of slight variations in the overhand length of the clamped supports. Consequently, highly localized vibration modes were displayed for configurations of microbeams with a small width, wide gap separation and tilt angle according to the ample response of the frequency peaks of the eigenstates. Furthermore, when studying the added mass effect of the perturbed system, higher resonant frequency shifts were noticeable for those highly localized vibration modes as was the case of the 4^{th} eigenstate. Nevertheless, the findings in the amplitude displacement of the eigenstates were not easily correlated as those exhibited by symmetrically coupled microcantilevers to suggest an enhancement in the sensitivity of the sensor. This was because of the disordered nature displayed by the amplitude response of asymmetrically coupled microbeams before and after adding a net mass onto the system.

The second microfabrication approach successfully built HMB devices by combining polycrystalline silicon and borophosphosilicate glass as structural and sacrificial materials, respectively. This was favourable for reducing the etching time while removing the embedded sacrificial layer to a few minutes given the high selectivity of the involved materials. Importantly, higher etching times can be achieved by doping the silicate glass using only phosphorous. It should be noted that the gap distance between the fabricated HMB resonators was limited by the resolution limit of the photomasks (1.5 μm) but mainly, by the ability to align them using the aligner equipment with a resolution limit of 1 μm. The fabrication scheme was simplified by implementing surface micromachining steps and employing only two photolithographic steps. Nevertheless, releasing the HMB devices from the substrate caused undercutting at the clamped supports. In this case, the coupling strength of the resonating system was firmly mitigated by the actuation scheme for driven into resonance the resonators response. Some devices exhibited active localized vibration modes, but the feasibility to fill them with fluidic solutions was constrained, and so the experimental measurements were limited to those devices in operational conditions and lower coupling strength.

The performance of the HMB devices was experimentally validated to work as a mass density and viscosity sensor while streaming sample solutions through them. The sensors demonstrated a linear tendency between the resonance frequency shifts of the resonators and the density of different samples such as solvents, organic solutions and alcoholic beverages in real-time. The extracted density of solutions was compared to data from commercial products showing a good correlation and importantly, the acquisition method made it possible to detect a mass responsivity of 7.4 Hz/pg. Also, we have found a correlation of the viscosity of samples as a function of increasing the Q-factor value of the resonators. Due to the non-monotonic energy dissipation of this type of devices, viscosity measurements were feasible in a short linear regime, between 1 cP to 2.6 cP, with a resolution of 0.15 cP. Hence, this work represents a step towards the development of a multiplexed platform capable of rapid monitoring of rheological properties of different fluidic samples.

Regarding material properties of the sensor, a structural material such as polysilicon has some advantages in comparison with silicon nitride devices. Deposition of polysilicon layers by the present fabrication scheme, resulted in low tensile strength structures with values between 800 to 1100 MPa, which prevented the deformation of the structures. Moreover, polysilicon can be easily

oxidized by different methods such as thermal oxidation or by direct streaming of oxidation agents. This advantage is of importance, i.e. in modifying the hydrophilic properties of the inner microfluidics walls to facilitate the filling of resonators with fluids of different viscosities. Another advantage of polysilicon is a reduction in sacrificial layer etching times to a few minutes.

The side over-etching effect on the third generation of HMB devices was reduced by using an additional photolithographic level to empty and release the resonators in two consecutive steps. This approach successfully proved the integration of polymer-based microfluidics at wafer level scale. However, this bonding strategy might be implemented nearly at the end of the manufacturing process to avoid any interference with the bulk micromachining steps when releasing the devices from the substrate. Further improvements should be considered for packaging the HMB devices at the wafer scale by using glass frit bonding strategies for instance, and using an intermediate layer to protect the surface of the microchannels.

The home-built experimental setup demonstrated the following achievements: i) integration of on-chip polymer microfluidics for injection of fluidic samples, ii) a throughput excitation methodology to drive the response of the resonators and iii) optical detection of the nanometric displacements of the devices.

Regarding the fluid delivery system integration, explanation and advice were provided for the proper on-chip integration of polymer-based microfluidics using three bonding strategies exploring polymer materials such as PDMS, SU-8 and SUEX. This included the sealing with good step coverage of microstructures with features that protruded out from the based substrate. However, for the second generation of HMB devices, the quality and durability of the bonding resulted unfavourable when working in vacuum conditions since the PDMS polymer is porous.

The filling capabilities of the embedded microchannels were successfully proven owing to the physical properties of the internal sidewalls, which presented low porosity and a high planarization level. The low intrinsic resistance of microchannels with higher cross sections facilitated the injection of fluidic samples. Likewise, the oxidation schemes of the HMB devices of the second and third generation demonstrated that thin oxide layers can improve the hydrophilicity of the microchannels inner surface. However, the high oxidation temperatures employed introduced compressive stress into the structural material of the resonators despite the robust design of the doubly clamped configuration.

The implemented optical readout allowed the efficient acquisition of the nanometric out-of-plane displacements of the HMB devices automatically. The parallel distribution of resonators allowed to freely moving along the array to capture the bending motion of resonators before and after injecting a sample solution. Although sequential detection of the beams was feasible, other detection systems might be useful for multiplexed measurements because the Michelson interferometer detection was limited to acquire the response of a single resonator. Future improvements on the detection system must be made to capture the response of all the resonators jointly taking into account other physical phenomena such as the diffraction effect produced by the distance gap between the resonators. Likewise, enhancing the frequency resolution of the detection system by implementing parametric

feedback oscillator methodologies and operating the devices in a moderate vacuum, can continuously improve the sensitivity of the HMB devices.

Importantly, the results of this Thesis work can be used for developing future biosensor platforms with multiple analyte detection capabilities by implementing mechanically coupled systems. Once a better understanding is elucidated about the highly localized vibration modes of asymmetrically coupled microbeams, a single input/output detection system could be implemented taking into account the coupling strength of the resonators. In this way, each microchannel can be adequately functionalized to detect a mass shift of the system on those vibration modes that are highly localized when streaming various analytes through each of the microfluidic channels.

Annex 1

Configuration and settings for the solver methods used in a Level Set Laminar Two-Phase Flow interface in order to optimize the resources and time of processing while computing a) 2D and b) 3D microfluidic simulations.

a)

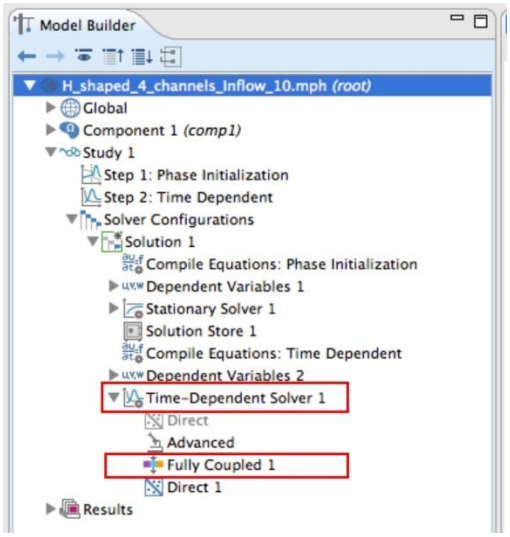

b)

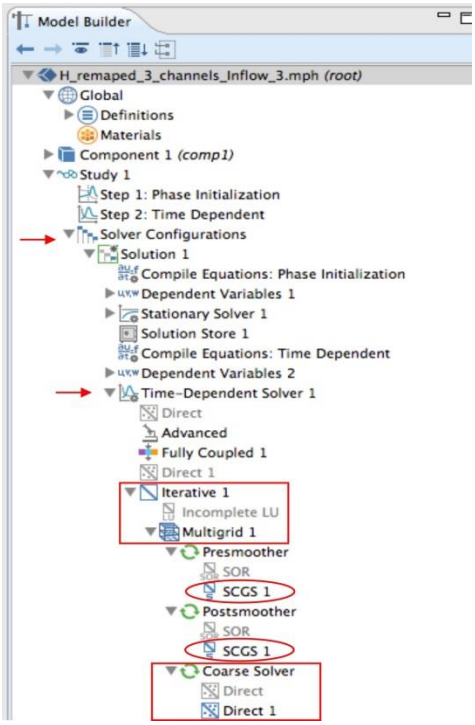

Configuration and settings for the solver methods used in a Level Set Laminar Two-Phase Flow interface in order to optimize the resources and time of processing while computing a) 2D and b) 3D microfluidic simulations.

a)

Fully Coupled settings
Nonlinear method: Constant (Newton)
Jacobian update: On every item iteration
Maximum number of iterations 4
Tolerance factor: 1

Time-dependent solver (BDF)
Steps taken by solver: free
Initial step: 0.001
Maximum step: 0.2
Event tolerance: 0.01

b)

Time-dependent solver (BDF)
Iterative **Error settings: Factor error estimate = 2, Maximum number of iterations = 1000**
Multigrid (Geometric type) **Iterations = 2** **Levels = 1** **Mesh coarsening factor = 2**
Multigrid options: **Presmoother = SCGS,** **Postsmoother = SCGS,** **Coarser Solver = Direct solver (PARDISO)**

Annex 2

Alignment masks for RUN8077

CNM788

HMB-BRID1

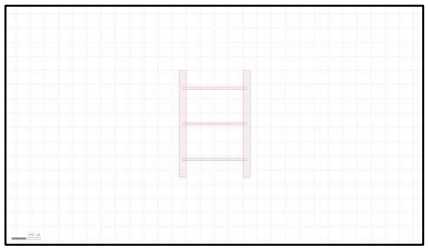

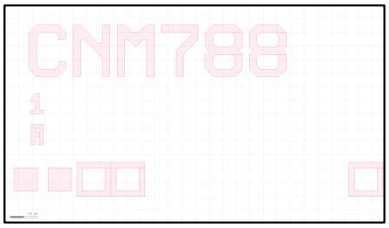

CNM788

HMB-HOLE2

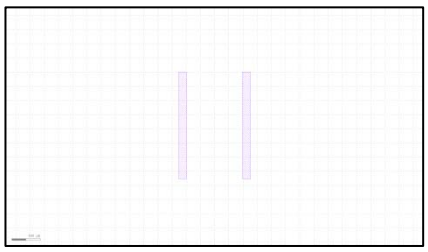

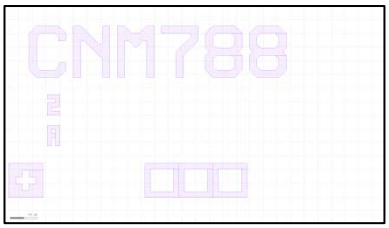

CNM788

HMB-OPEN3

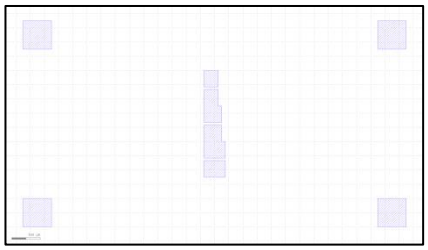

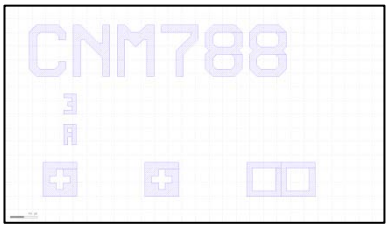

CNM788

HMB-GRID6

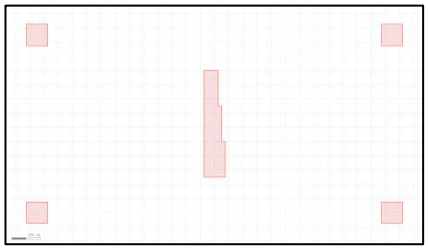

CNM788

HMB-SU8A

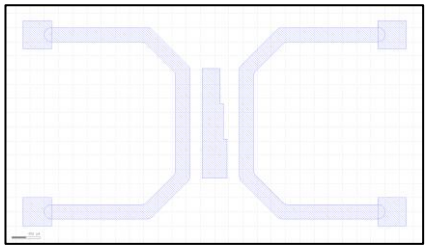

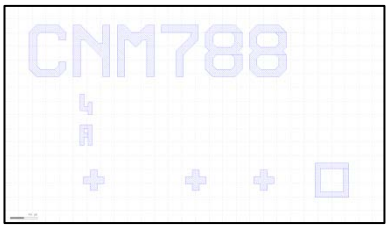

CNM788

HMB-SU8A

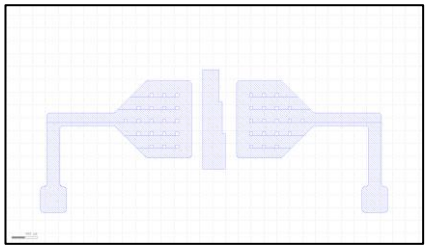

CNM788

HMB-SU8B